

Investigating Self-Supervised Image Denoising with Denaturation

Hiroki Waida^{*1}, Kimihiro Yamazaki², Atsushi Tokuhisa³, Mutsuyo Wada², and
Yuichiro Wada^{†2,4}

¹Department of Mathematical and Computing Science, Tokyo Institute of Technology, 2-12-1
Ookayama, Meguro-ku, Tokyo, 152-8550, Japan

²Fujitsu Limited, 4-1-1 Kamikodanaka, Nakahara-ku, Kawasaki-shi, Kanagawa, 211-8588, Japan

³RIKEN Center for Computational Science, 7-1-26 Minatojima-minami-machi, Chuo-ku, Kobe,
Hyogo, 650-0047, Japan

⁴RIKEN Center for Advanced Intelligence Project, Nihonbashi 1-chome Mitsui Building, 15th
floor, 1-4-1 Nihonbashi, Chuo-ku, Tokyo, 103-0027, Japan

Abstract

Self-supervised learning for image denoising problems in the presence of denaturation for noisy data is a crucial approach in machine learning. However, theoretical understanding of the performance of the approach that uses denatured data is lacking. To provide better understanding of the approach, in this paper, we analyze a self-supervised denoising algorithm that uses denatured data in depth through theoretical analysis and numerical experiments. Through the theoretical analysis, we discuss that the algorithm finds desired solutions to the optimization problem with the population risk, while the guarantee for the empirical risk depends on the hardness of the denoising task in terms of denaturation levels. We also conduct several experiments to investigate the performance of an extended algorithm in practice. The results indicate that the algorithm training with denatured images works, and the empirical performance aligns with the theoretical results. These results suggest several insights for further improvement of self-supervised image denoising that uses denatured data in future directions.

1 Introduction

Image denoising is a task to predict the clean image of high-resolution from an observation perturbed by some random noise, which is recognized as an important topic for decades [1, 2, 3]. [2, 3] provide significant improvement for this task by making use of the following components:

^{*}H. Waida did this work while he was an internship student at Fujitsu Ltd.

[†]Corresponding author. E-mail: wada.yuichiro@jp.fujitsu.com

[2] show the power of deep learning for supervised denoising tasks, and [3] focus on a strategy that learns noise patterns from multiple pairs of images whose resolution may not be necessarily high enough. After [3] has presented this self-supervised strategy, the combination of these components has been actively studied: for instance, [4, 5] proposed alternative techniques for generating a pair of noisy images from a single observation, and [6, 7] introduced denoising methods that learn the noise pattern from a test image itself in a self-supervised manner. The method of [3] is theoretically well-investigated in [8, 5]. [8] show that the empirical method studied by [3] implicitly utilizes a theoretical relation between self-supervised denoising and supervised denoising. [5] also consider theory on the method of [3] under general assumptions for noise distributions.

From practical viewpoints, denoising of images collected from a device is a useful technique before handling other operations using the data. For instance, Cryo-Electron Microscopy (Cryo-EM) collects 2D projection images of target biomolecules [9]. As [10] point out, those images are not only noisy but also denatured due to an electron beam. It is important to denoise from the 2D projection images, since it is shown that the denoised Cryo-EM images can help to reconstruct 3D structures of the biomolecules [11, 12]. We note that the reconstructed structures have a potential to lead biological significance, e.g., a biological finding to develop anti-cancer drugs [13]. As another example, Magnetic Resonance Imaging (MRI) collects noisy images with kind of denaturation, and the corresponding self-supervised denoising problems are investigated in [14, 15]. Considering this background, understanding the ability of self-supervised denoising using denatured images is a crucial topic.

On the other hand, the seminal work by [3] designed a statistical modeling for a noisy image whose conditional expectation with respect to the clean counterpart coincides with the clean one. Therefore, the modeling of [3] cannot apply to the situation in which the clean image can be denatured by some transformation. In the field of self-supervised denoising, several authors have shown the empirical advantages of their proposed methods for noisy images with denaturation [16, 15]. However, it is not theoretically investigated whether some method based on the methodology of [3] can deal with denoising problems in the presence of some general and unknown transformation to training images. Addressing this issue is important to fully utilize the methodology of [3] under general settings.

In this paper, we address the above issue from both the theoretical and empirical viewpoints. We study a self-supervised denoising algorithm for estimating the fixed target image of high-resolution from denatured training images contaminated by noise. In particular, our approach focuses on a simple extension from the framework called *Noise2Noise* [3] to facilitate learning by making use of the common features among the denatured images. The contributions of this paper are summarized below:

- We show that similarly to the theoretical results presented in [8, 5], the algorithm extended from [3] has the theoretical guarantees for a population loss minimizer.
- In addition, we derive a statistical guarantee for an empirical risk minimizer. The guarantee holds under the non-asymptotic statistical theory, which has not been addressed yet in the context of self-supervised denoising. The result reveals both the quantitative performance and limitations of the algorithm.

- Building on the theoretical results, we instantiate the self-supervised denoising algorithm termed *Denatured-Noise2Noise* (DN2N) to investigate the empirical aspects of the algorithm. In the experiment that uses toy datasets with denaturation and noise, we confirm the consistency between the theoretical analysis and empirical performance of DN2N. We also show efficiency of DN2N for the following two benchmark datasets: MRI and Cryo-EM image datasets.

2 Preliminaries

We begin by formulating the problem setting and reviewing some background on self-supervised denoising.

2.1 Problem Setting

The aim of this study is to analyze a self-supervised image denoising algorithm extended from the basic framework of [3] to leverage denatured noisy images. To this end, we present the fundamental problem setting in this paper.

Let (Ω, P) be a probability space, and let $\tau : \Omega \rightarrow (0, T]$ be a random variable indicating time. Let $\mathbf{y} : \Omega \times [0, T] \rightarrow \mathbb{R}^d$ be a continuous-time stochastic process. This stochastic process represents the time-series of denatured noisy images. We aim to make use of information derived from the denatured images to learn a neural-network-based model f to predict as $f(\mathbf{y}_0) \approx \mathbf{x}_0$, where \mathbf{x}_0 is unknown during both the training and test phases. We note that we consider the fixed design for the estimation problem: in fact, the target image \mathbf{x}_0 is fixed throughout the setting, and the training images are utilized to estimate the realization \mathbf{x}_0 .

The difficulty of this setup arises from the condition that the sequence is denatured, meaning that for a mapping $\phi : \mathbb{R}^d \times [0, T] \rightarrow \mathbb{R}^d$, the clean image \mathbf{x}_t corresponding to \mathbf{y}_t is represented by $\phi_t(\mathbf{x}_0)$, where note that $\phi_0(\mathbf{x}_0) = \mathbf{x}_0$ (the formal definition is introduced in Assumption 1 in Section 4.1). For instance, when we choose to model the noise ε_t as the multivariate standard normal distribution, the statistical modeling for \mathbf{y}_t may be written as

$$\mathbf{y}_t = \phi_t(\mathbf{x}_0) + \varepsilon_t \quad \forall t \in [0, T]. \quad (1)$$

When $T = 0$, (1) is reduced to a modeling studied by [3]. Besides, the modeling recovers that of [14] when ϕ_t represents the deformation transforms for images. From statistical viewpoints, this problem may be resolved by estimating ϕ_t directly under the regression modeling. Unfortunately, this strategy cannot apply to our setting since the clean data \mathbf{x}_0 is unknown as in the literature on self-supervised denoising [3, 6, 14].

2.2 Background from Technical Viewpoints

We next discuss some background of the previous self-supervised denoising methods to see what to be investigated for achieving our goal.

Several self-supervised denoising methods using many images have been proposed in a line of research [3, 4, 17, 18, 5, 19, 20, 21, 22, 23, 24]. Several existing frameworks proposed by [4, 17, 5] are built on a method proposed by [3]. Formally, [3] formulate their framework as minimization of the objective

$$\mathbb{E}_{\mathbf{y}, \mathbf{y}'}[\|\mathbf{g}(\mathbf{y}) - \mathbf{y}'\|_2^2],$$

where \mathbf{y} and \mathbf{y}' are random noisy images, and \mathbf{g} is a function that predicts the clean image \mathbf{x}_0 . Note that [3] consider more general loss function in their method (see Eq.(2) in [3]), while we primarily focus on the ℓ_2 distance in our work. Here, let us rewrite the objective function of [3] as the expectation of conditional expectation for \mathbf{x}_0 , that is,

$$\mathbb{E}_{\mathbf{y}, \mathbf{y}'}[\|\mathbf{g}(\mathbf{y}) - \mathbf{y}'\|_2^2] = \mathbb{E}_{\mathbf{x}_0}[\mathbb{E}_{\mathbf{y}, \mathbf{y}'}[\|\mathbf{g}(\mathbf{y}) - \mathbf{y}'\|_2^2 | \mathbf{x}_0]].$$

Let us focus on the loss $\mathbb{E}_{\mathbf{y}, \mathbf{y}'}[\|\mathbf{g}(\mathbf{y}) - \mathbf{y}'\|_2^2 | \mathbf{x}_0]$. In fact, Theorem 1 in [5] implies that under some mild conditions, this loss function has the learning theory guaranteeing the equality

$$\mathbb{E}_{\mathbf{y}, \mathbf{y}'}[\|\mathbf{g}(\mathbf{y}) - \mathbf{y}'\|_2^2 | \mathbf{x}_0] = \mathbb{E}_{\mathbf{y}}[\|\mathbf{g}(\mathbf{y}) - \mathbf{x}_0\|_2^2 | \mathbf{x}_0].$$

However, it is pointed out by [4] that preparing pairs of random variables $(\mathbf{y}, \mathbf{y}')$ is not realistic in practical situations. We also face an issue similar to [4] when attempting to apply the method of [3] directly to our setting, since we consider a case that the sufficient amount of such pairs may not be available.

If we substitute \mathbf{y}' for a denatured noisy image \mathbf{y}_τ whose clean image is represented as $\phi_\tau(\mathbf{x}_0)$, then following a similar idea to [3], we can define the loss $\mathbb{E}[\|\mathbf{g}(\mathbf{y}_0) - \mathbf{y}_\tau\|_2^2 | \mathbf{x}_0]$. A variant of this loss has already been employed in the context of biological image denoising [25]. Recall that [5, Theorem 1] imply under some conditions that optimizing the loss is equal to minimizing $\mathbb{E}[\|\mathbf{g}(\mathbf{y}_0) - \phi_\tau(\mathbf{x}_0)\|_2^2 | \mathbf{x}_0]$. This implies that learning with this loss function is affected by the changes in the denatured images, which results in worsening the quality of prediction after the stage of training. This loss of information also makes it hard to apply a recent approach explored by [26] to this setting.

We also mention that single image denoising method have also been proposed in [27, 6, 28, 29, 7]. [6] propose a self-supervised method that uses only the noisy image \mathbf{y}_0 to learn denoising models. [28] propose a fast method with a theoretical background. However, [28] builds their theory on the assumption that a noisy image is defined as the summation of a clean image and some additive random variable. Meanwhile, we aim to investigate the performance of self-supervised denoising under more general settings. [7] also improve the running time by considering to leverage the framework of [3]. Note that different from [7], we study the properties of the methodology of [3] in a scenario where denatured images are available for training.

3 A Time-Aware Denoising Loss

Motivated by the discussion in Section 2.2, we consider to utilize denatured noisy image to perform self-supervised denoising without loss of much information from \mathbf{x}_0 . Following a similar idea

to [14, 16, 15], we consider to extend a framework of [3] to suppress the loss of information due to the general mapping ϕ_t and leverage the remained information for enhancing training. As we will see in the later section, this approach also enables to ensure a theoretical guarantee for training (see Section 4).

3.1 Definition

The basic strategy of our analysis is to introduce additional time variable to a self-supervised denoising framework. Let $f : \mathbb{R}^d \times [0, T] \rightarrow \mathbb{R}^d$ be a training model, where we aim to train f such that $f(\mathbf{y}_0, \tau) \approx \phi_\tau(\mathbf{x}_0)$. We first focus on the following self-supervised learning objective extended from [3]:

$$\mathbb{E}_{\mathbf{y}, \tau} [\|f(\mathbf{y}_0, \tau) - \mathbf{y}_\tau\|_2^2 | \mathbf{x}_0]. \quad (2)$$

The objective function (2) is a simple extension from the framework called *Noise2Noise* [3], where we add time information due to our problem setting.

After training, we predict the target clean image \mathbf{x}_0 by letting $t = 0$ in its input, namely $f(\mathbf{y}_0, 0)$. Intuitively, the denatured information in the images \mathbf{y}_t , $t \in (0, T]$ are used for learning how to trace back to \mathbf{x}_0 from the denatured but clean image $\phi_t(\mathbf{x}_0)$. We note that a similar setting for denoising tasks is considered in [30], where [31, 16, 32] also study utilization of deep learning in the same context as [30]. One of the notable strengths of the extended approach in (2) is that we can make use of denatured images directly without combining additional techniques. In fact, let us recall that [4] use some operations such as some data augmentation technique, and [5] introduce a method to construct new images by drawing pixels randomly from the noisy image. Whereas in (2), by utilizing information of similarity existing in the sequence of images $\{\mathbf{y}_t\}$ instead, we can reduce the cost drastically.

As a remark, the loss function (2) is related to some losses proposed in several previous works [14, 16, 15, 33]. We discuss this point in Section 3.2.

3.2 Relations to the Previous Work

To the best of our knowledge, among the existing literature on denoising using sequences of noisy images, the work by [14] is closely relevant to our problem setting. [14] utilize a framework referred to as *Self2Self* [6] to denoise deformed noisy images and then correct deformation of the predicted images by applying a sampling technique for grids in images. [14] empirically verify that the performance of their method overwhelms that of [6]. However, the theoretical analysis showing what will be reconstructed as the final output from the model trained according to the method of [14] is an open problem. We note that the target of our work is the methodology of *Noise2Noise* [3], different from [14]. Moreover, [14] investigate in a setting that underlying clean images are deformed. Meanwhile, in this paper, we address a broader problem by treating ϕ_t as a general mapping, which can be non-linear transformations.

We also discuss the previous works [16, 15] related to our approach. [16] introduce a method to learn how to remove both mosaic and noise components simultaneously, where their approach

minimizes a norm function so that a model can learn how to transform an image into others. The main difference from [16] is that we additionally input the time variable for the model f . [15] tackle the self-supervised denoising with deformed noisy medical images by extending a framework of [3]. However, [15] mainly focus on the empirical aspects of their method.

Here we also note that (2) has similarity to the method called *Denoising Diffusion Probabilistic Model* [33]. [33] utilize the mechanism of denoising to generate high quality images. Meanwhile, (2) has the following main difference in its mechanism from the loss of [33]: (2) is built on the idea that the reconstruction $f(\mathbf{y}_0, \tau)$ is made close to the denatured noisy image \mathbf{y}_τ , while [33] consider to fill the gap between prediction and noise itself. Note that the combination of MRI denoising and the generative model of [33] is also recently paid attention in [34].

4 Theoretical Analysis

A question to the previous section is whether the framework has some theoretical guarantee. In this section, we first give a positive answer to this question. Note that in this section, the random variables $\{\mathbf{y}_{0,j}\}_{j=0}^M$, $\{\tau_i\}_{i=0}^N$, and $\{\mathbf{y}_{t,j}\}_{j=0}^M$ are identically distributed within each sequence of random variables, and all the random variables are independent, where $\mathbf{y}_{0,0} = \mathbf{y}_0$, $\tau_0 = \tau$, and $\mathbf{y}_{t,0} = \mathbf{y}_t$. Furthermore, the clean image \mathbf{x}_0 is fixed.

4.1 On Population Risk Minimizers

The theoretical guarantee of the time-aware denoising algorithm is mainly based on the following conditions.

Assumption 1 (Assumptions on data). *The following conditions hold:*

- (A) *It holds that $\mathbb{E}[\mathbf{y}_t | \mathbf{x}_0] = \phi_t(\mathbf{x}_0)$ for any $t \in [0, T]$.*
- (B) *For any $\mathbf{x} \in \mathbb{R}^d$, the function $\phi_t(\mathbf{x})$ in variable t is right-continuous at $t = 0$.*
- (C) *For any $t, t' \in [0, T]$ satisfying $t \neq t'$, \mathbf{y}_t and $\mathbf{y}_{t'}$ are independent if they are conditioned on \mathbf{x}_0 .*

Note that the condition (A) of Assumption 1 extends assumptions considered in [3, 5] to a setting where we need to deal with the mapping ϕ_t together. This condition means that the noisy image \mathbf{y}_t observed at each time t is denatured by some mapping ϕ_t and perturbed by some noise. Note that if we only consider the case that $T = 0$ and ϕ_0 is the identity mapping, then this modeling can recover the conditions studied in [3, 5]. Also note that the condition (A) of Assumption 1 includes the modeling considered in [14] as a special case. Based on these conditions, similar to usual least-squares problems (see e.g. [35]), we can ensure that minimization for (2) yields the desired result.

Proposition 1. *Suppose that all the conditions in Assumption 1 hold. Suppose also that a minimizer f^* of the objective function (2) over all measurable mapping from $\mathbb{R}^d \times [0, T]$ to \mathbb{R}^d meets the*

condition that $f^*(\tilde{\mathbf{y}}_0, t)$ is right-continuous at $t = 0$ almost every $\tilde{\mathbf{y}}_0 \in \mathbb{R}^d$ with its probability distribution. Then, the minimizer f^* meeting the conditions above satisfies

$$\mathbb{E}_{\mathbf{y}_0}[f^*(\mathbf{y}_0, 0)|\mathbf{x}_0] = \mathbf{x}_0. \quad (3)$$

Proposition 1 extends the theory on *Noise2Noise* [3] shown in Section 3.1 of [8] and Theorem 1 of [5] to a setting that observed data may contain denaturation. The proof of Proposition 1 is deferred to Appendix A.1.

4.2 On Empirical Risk Minimizers

Once obtaining the theoretical justification for the population minimizer, it is also important to investigate how close the prediction $\hat{\mathbf{x}}_0$ defined with the empirical risk minimizer and the true clean \mathbf{x}_0 are. We address this problem by evaluating the Euclidean norm between them. To present the result, let us introduce the empirical loss

$$\frac{1}{MN} \sum_{j=1}^M \sum_{i=1}^N \|f(\mathbf{y}_{0,j}, \tau_i) - \mathbf{y}_{\tau_i,j}\|_2^2. \quad (4)$$

Let \hat{f} be the Empirical Risk Minimizer (ERM) of (4) over a class of Lipschitz functions, where note that we select this class since the learning theory of Lipschitz spaces is well-investigated in [36]. We define the predicted image as $\hat{\mathbf{x}}_0 = \frac{1}{M} \sum_{j=1}^M \hat{f}(\mathbf{y}_{0,j}, 0)$. Then, the following evaluation holds:

Theorem 1. *Let $U = [0, 1]^d$, $B_1 = \sqrt{d}$, and $L > 0$. Let $\mathcal{F} = \{f : U \times [0, 1] \rightarrow \mathbb{R}^d | f(\mathbf{0}, 0) = \mathbf{0}, f = (f_1, \dots, f_d), f_1, \dots, f_d \text{ are } L\text{-Lipschitz}\}$, where f_k is L -Lipschitz in the sense that $|f_k(\mathbf{u}_1, t_1) - f_k(\mathbf{u}_2, t_2)| \leq L\sqrt{\|\mathbf{u}_1 - \mathbf{u}_2\|_2^2 + |t_1 - t_2|^2}$ holds for any $\mathbf{u}_1, \mathbf{u}_2 \in U$ and $t_1, t_2 \in [0, 1]$. Suppose that there exists $\hat{f} \in \mathcal{F}$ such that \hat{f} is the ERM (4) over \mathcal{F} . Suppose also that there exists some $B_2 \geq 0$ such that for every $i \in \{1, \dots, N\}$ and $j \in \{1, \dots, M\}$, $\|\mathbf{y}_{\tau_i,j}\|_2 \leq B_2$ holds almost surely. We further assume that $\mathbf{y}_{\tau_1,j}, \dots, \mathbf{y}_{\tau_N,j}$ are i.i.d. for each $j \in \{1, \dots, M\}$. Let $\delta > Me^{-N}$, and $B = (L\sqrt{B_1^2 + 1} + B_2)^2$. Then, under Assumption 1, there exists a constant $C > 0$ that is independent of M, N, δ such that with probability at least $1 - 4\delta$, it holds for the prediction $\hat{\mathbf{x}}_0 = \frac{1}{M} \sum_{j=1}^M \hat{f}(\mathbf{y}_{0,j}, 0)$ that*

$$\|\hat{\mathbf{x}}_0 - \mathbf{x}_0\|_2^2 \leq C(E_{\mathcal{F}} + G_{\phi} + L^2\mathbb{E}[\tau^2] + N^{-\frac{1}{2}} + \sqrt{(M \wedge N)^{-1} \log(M/\delta)}),$$

where $E_{\mathcal{F}} = \inf_{f \in \mathcal{F}} \mathbb{E}[\|f^*(\mathbf{y}_0, \tau) - \mathbf{y}_{\tau}\|_2^2]$, and $G_{\phi} = \|\mathbb{E}_{\tau}[\phi_{\tau}(\mathbf{x}_0)] - \mathbf{x}_0\|_2^2$.

The proof of Theorem 1 basically relies on the notion called *Rademacher complexity* [37] and several concentration inequalities (see e.g., [38, 39]). The detailed proof of Theorem 1 is deferred to Appendix A.2. To the best of our knowledge, the theoretical analysis dealing with the quantitative evaluation of the prediction made by the ERM is little investigated in the context of self-supervised denoising. Here we describe several interpretations of this theorem. The upper bound consists of four different kinds of quantities: the approximation error $E_{\mathcal{F}}$, the gap term G_{ϕ} ,

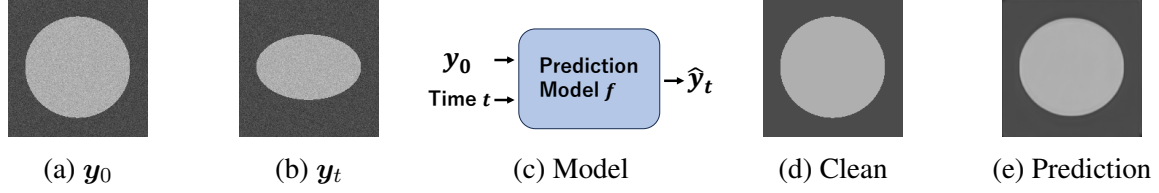


Figure 1: Overview of our method. (1a) and (1b): Examples of training images for our method, where y_t , $t > 0$ (resp. y_0) denotes a denatured (resp. non-denatured) noisy image at time t (resp. time 0), and the circle in (1a) is degenerated into the ellipse in (1b) as t increases. (1c): Our prediction model f based on a deep neural network, where in the prediction phase, the prediction is given by \hat{y}_0 . (1d): Corresponding clean image x_0 for y_0 . (1e): Prediction result \hat{x}_0 by our method for x_0 . The detail of the setting for the simulation in (1e) can be found in Section 6.1.3.

the averaged squared-time $\mathbb{E}[\tau^2]$, and some constant terms that will vanish if $M, N \rightarrow \infty$. The approximation error depends on the hardness of the denoising task and is expected to be small as long as \mathcal{F} is a sufficiently large class. The gap term measures to what extent the transformed image $\phi_t(x_0)$ is far apart from the clean x_0 on average, which depends on the property of ϕ_t and x_0 . The average time reveals some aspect of what kind of denatured dataset we use, since this term can become larger as the time for collecting images tend to be longer. Therefore, Theorem 1 implies that as long as both the denoising task and dataset are not too hard to deal with, training with the loss function (4) leads to successful results with high probability.

5 Denatured-Noise2Noise

The previous section reveals both the guarantee and limitation of the algorithm using (2). We next move on to investigation of the empirical perspectives. To this end, we employ the loss (2) as the backbone of the self-supervised denoising framework we study. In addition, we incorporate several techniques and regularization terms to enhance the performance. Since the main loss function is extended from the existing loss called *Noise2Noise* [3] to deal with denaturation in observed data, we call this framework *Denatured-Noise2Noise* (DN2N). We note that an illustration for the diagram can be found in (1c) of Figure 1.

Transforming Input Images In practice, we often deal with the case that both M and N are relatively small. As seen in Theorem 1, in such situations the generalization performance of denoising models can be worsened. To overcome this problem, we consider to transform data y_0 to create multiple noisy images. More precisely, let m be a random mapping on \mathbb{R}^d such that for any y , the output $m(y)$ is defined as $m(y) = y + \varepsilon$, where $y \in \mathbb{R}^d$, and ε is a noise random variable that is independent of any other random variables and satisfies $\mathbb{E}[\varepsilon|x_0] = \mathbf{0}$. Let m' be another mapping defined as in m with random noise ε' independently and identically distributed with ε . Using this mapping, we redefine the loss function as

$$\mathcal{L}_D(f) = \mathbb{E}_{y, \tau, m} [\|f(m(y_0), \tau) - m'(y_\tau)\|_2^2 | x_0].$$

Note that this additional noise does not violate Assumption 1 by the definition. We remark that the approach that considers to add extra noise to the input noisy image has been utilized by several previous works [40, 18, 19]. Notably, we find that the existence of the additional noise also influences the performance of DN2N that takes denatured images as the inputs (see Section 6.4).

In training, we minimize the empirical risk

$$\widehat{\mathcal{L}}_D(f) = \frac{1}{LMN} \sum_{k=1}^L \sum_{j=1}^M \sum_{i=1}^N \|f(\mathbf{m}_k(\mathbf{y}_{0,j}), \tau_i) - \mathbf{m}'_k(\mathbf{y}_{\tau_i,j})\|_2^2, \quad (5)$$

where $\{\mathbf{m}_k\}_{k=1}^L$ and $\{\mathbf{m}'_k\}_{k=1}^L$ are random transforms defined with i.i.d. random noise $\{\varepsilon_k\}_{k=1}^L$ and $\{\varepsilon'_k\}_{k=1}^L$.

Averaging Loss In addition to the above problem, we also need to overcome the issue that the denaturation levels of data may deteriorate the denoising performance of (2). Toward addressing the issue, we take one step into making use of more information contained in the denatured images. Since the learning process is affected by both the denaturation and noise in the training images, we consider to alleviate only the noise and learn some structure of the denaturation. Following a similar approach to the classical averaging technique commonly referred to as *2D classification* [41, 42] in Cryo-EM image analysis, we further enforce the denoising model to incorporate less-noisy image constructed by averaging a series of denatured noisy images $\{\mathbf{y}_{\tau_i}\}_{i=1}^N$. We define the averaging loss as

$$\mathcal{L}_A(f) = \mathbb{E} \left[\frac{1}{M} \sum_{j=1}^M \left\| \frac{1}{N} \sum_{i=1}^N f(\mathbf{m}(\mathbf{y}_{0,j}), \tau_i) - \bar{\mathbf{y}}_j \right\|_2^2 \right],$$

where $\bar{\mathbf{y}}_j = \frac{1}{N} \sum_{i=1}^N \mathbf{m}'(\mathbf{y}_{\tau_i,j})$, and the expectation is taken for all the random variables. Then, using \mathbf{m}_k and \mathbf{m}'_k in (5), the empirical loss is also defined as

$$\widehat{\mathcal{L}}_A(f) = \frac{1}{LM} \sum_{k=1}^L \sum_{j=1}^M \left\| \frac{1}{N} \sum_{i=1}^N f(\mathbf{m}_k(\mathbf{y}_{0,j}), \tau_i) - \frac{1}{N} \sum_{i=1}^N \mathbf{m}'_k(\mathbf{y}_{\tau_i,j}) \right\|_2^2.$$

Training and Prediction The final version of the empirical loss in the denoising module is

$$\widehat{\mathcal{L}}_T(f) = \widehat{\mathcal{L}}_D(f) + \frac{\mu}{LMN} \cdot \widehat{\mathcal{L}}_A(f),$$

where $\mu \geq 0$ is a hyperparameter to be tuned. Note that in the above definition, we further multiply the coefficient $(LMN)^{-1}$ to $\mu \widehat{\mathcal{L}}_A(f)$ to control the effect of the regularizer to the main loss $\widehat{\mathcal{L}}_D(f)$, depending on the number of noisy images available. Let $\hat{f} \in \operatorname{argmin}_{f \in \mathcal{F}} \widehat{\mathcal{L}}_T(f)$, where \mathcal{F} is a space of denoising models. After training with (5), we predict the non-denatured clean image by

$$\hat{x}_0 = \frac{1}{KM} \sum_{i=1}^K \sum_{j=1}^M \hat{f}(\mathbf{y}_{0,j} + \varepsilon_i, 0), \quad (6)$$

where $K \in \mathbb{N}$. Note that [6] also propose an empirical technique that averages outputs from a model to produce the final prediction. [6] particularly utilize *dropout* [43] at the stage of inference. Meanwhile, we consider additive random noise, different from [6].

6 Experiments

We conduct the following three numerical experiments to demonstrate the performance of DN2N: *Expt.1*, *Expt.2*, and *Expt.3*. We describe the detail of each experiment from Section 6.1 to Section 6.3. The purpose of the first experiment is to evaluate the consistency between our analytical result in Section 4 and the prediction performance of our method on toy datasets. The second experiment is intended to quantitatively compare our method to existing state-of-the-art methods for an MRI image dataset under a setting similar to [14]. The goal in the third experiment is to qualitatively evaluate the performance of our method by a Cryo-EM image dataset, where no clean image is available for the evaluation. In Section 6.4, we explain our implementation, the detail of the settings, and the hyperparameter tuning.

Throughout all the experiments except *Expt.3*, following [3, 6, 5], we evaluate the prediction performance of our method on the noisy toy dataset by two standard metrics in vision domain: Peak Signal to Noise Ratio (PSNR) (see e.g., [44]) and Structural Similarity Index Measure (SSIM) [45]. Note that we use the package called `scikit-image` [46] for implementation of these metrics. In the experiments, we use four NVIDIA V100 GPUs combined with two Intel Xeon Gold 6148 processors.

6.1 Expt.1: Evaluation of Theoretical Results using Toy Datasets

6.1.1 Setting

We firstly craft two clean image datasets. All the images in the two datasets are gray-scale with the size 192×192 , and the number of images in each dataset is 25. The two datasets share the same clean image at time $t = 0$ (see the clean image in (1d) of Figure 1), while the denaturing speed is different. Let $\mathcal{D}_1^{\text{toy}}$ and $\mathcal{D}_2^{\text{toy}}$ denote the two clean datasets. In $\mathcal{D}_1^{\text{toy}}$, a circle in (1d) is denatured *slowly* into an ellipse as the time index t increases, whereas in $\mathcal{D}_2^{\text{toy}}$, the denaturing speed is *faster*; the formal definitions of $\mathcal{D}_1^{\text{toy}}$ and $\mathcal{D}_2^{\text{toy}}$ will be presented in the subsequent paragraph below. Following [47], we then add Poisson noise with the hyperparameter $\lambda > 0$ and Gaussian noise with the standard deviation σ for both the clean datasets; the formal definitions of the noises are also deferred to the paragraph below. Two example images of $\mathcal{D}_2^{\text{toy}}$ with Poisson-Gaussian noises are displayed in (1a) and (1b) of Figure 1.

We then describe the formal definitions of the toy dataset and noises in the following paragraphs separately.

Toy Dataset We introduce the definitions of two clean datasets: $\mathcal{D}_1^{\text{toy}} = \{\mathbf{x}_0, \mathbf{x}_1^{(1)}, \dots, \mathbf{x}_t^{(1)}, \dots, \mathbf{x}_T^{(1)}\}$ and $\mathcal{D}_2^{\text{toy}} = \{\mathbf{x}_0, \mathbf{x}_1^{(2)}, \dots, \mathbf{x}_t^{(2)}, \dots, \mathbf{x}_T^{(2)}\}$, where $\mathbf{x}_t^{(s)}$ ($t > 0$) denotes denatured clean image

Table 1: Results of Expt.1: evaluation of predicting performance by our method on toy image datasets with different denaturing speed and noise intensity. The word “Slow” (resp. “Fast”) represents the denaturing speed. The higher number means the better performance in both PSNR and SSIM metrics.

(λ, σ)	(25, 10)		(10, 10)		(25, 25)		(10, 25)	
	PSNR	SSIM	PSNR	SSIM	PSNR	SSIM	PSNR	SSIM
Slow	34.39	0.976	34.77	0.979	34.62	0.974	34.21	0.973
Fast	27.03	0.937	27.28	0.936	27.69	0.937	27.70	0.938

with time index t in $\mathcal{D}_s^{\text{toy}}$, \mathbf{x}_0 is non-denatured clean image, and $T = 24$. The clean image \mathbf{x}_0 is visualized in (1d) of Figure 1. Let us define the horizontal (resp. vertical) axis as i (resp. j) axis to the clean image. In (1d), the coordinates at the bottom-left, bottom-right, top-right, and top-left pixel are defined by $(1, 192)$, $(192, 192)$, $(192, 1)$, and $(1, 1)$, respectively. In addition, let $(97, 97)$ denote the coordinates of the *center* pixel in \mathbf{x}_0 . The gray circled region is defined by

$$\mathcal{R}_t := \left\{ (i, j) \in \mathbb{N}^2 \mid \frac{(i - 97)^2}{a_t^2} + \frac{(j - 97)^2}{1^2} \leq \left(\frac{3}{4} \cdot \frac{\ell}{2} \right)^2 \right\}, \quad (7)$$

where $\ell = 192$ and $a_0 = 1$. The remaining region in \mathbf{x}_0 is defined by \mathcal{R}_0^c . In Expt.1, we design two toy clean image datasets, in both of which the gray circle in \mathbf{x}_0 becomes an gray ellipse as the time index t increases. The difference is the denaturing speed, and the ellipse region in \mathbf{x}_t ($t > 0$) is defined by \mathcal{R}_t of (7), whose

$$a_t = \begin{cases} \log(\sqrt{t} \cdot (\sqrt{e} - e)/T + e), & \text{if } \mathbf{x}_t \in \mathcal{D}_1^{\text{toy}}, \text{ i.e., “slow” case,} \\ \exp(-t^{1.1} \log 2/T), & \text{if } \mathbf{x}_t \in \mathcal{D}_2^{\text{toy}}, \text{ i.e., “fast” case,} \end{cases} \quad (8)$$

whereas the remaining region is defined by \mathcal{R}_t^c . Note that $a_t = 1$ in both cases of (8) if $t = 0$. Furthermore, (i, j) -th pixel value in \mathbf{x}_t , denoted by $x_t(i, j)$, is defined as follows:

$$x_t(i, j) = \begin{cases} 175, & \text{if } (i, j) \in \mathcal{R}_t, \\ 75, & \text{if } (i, j) \in \mathcal{R}_t^c. \end{cases}$$

Poisson-Gaussian Noise We follow [47] to define a noisy image \mathbf{y} with the Poisson-Gaussian noise as follows: $\mathbf{y} = \lambda^{-1}\mathbf{z} + \boldsymbol{\delta}$, where \mathbf{x} is a clean image, λ is a positive hyperparameter, $\boldsymbol{\delta} \sim \mathcal{N}(\mathbf{0}, \sigma^2 \mathbf{I})$, $\mathcal{P}(\beta)$ is the Poisson distribution with parameter β , and $\mathbf{z} \sim \mathcal{P}(\lambda \cdot \mathbf{x})$. Note that [47] further approximate the formulation to a Gaussian noise model. Meanwhile, we use the modeling [47] initially consider.

6.1.2 Result and Discussion

The results are shown in Table 1. For all the pairs (λ, σ) in the table, DN2N works better for the datasets with slow denaturation, compared to the fast denaturation datasets. This tendency positively supports the theoretical finding in Theorem 1.

Table 2: Results of Expt.2: performance comparison between our method and three state-of-the-art methods using five persons’ time series MRI images from ACDC. The best performance is in bold font.

Method	ID 1		ID 2		ID 3		ID 4		ID 5	
	PSNR \uparrow	SSIM \uparrow	PSNR	SSIM	PSNR	SSIM	PSNR	SSIM	PSNR	SSIM
BM3D	22.29	0.743	23.32	0.722	23.35	0.752	18.12	0.687	23.48	0.741
N2F	22.93	0.754	23.64	0.749	23.80	0.749	20.31	0.720	23.63	0.718
D2S	23.92	0.807	24.80	0.752	25.04	0.784	21.11	0.778	24.83	0.777
DN2N (ours)	23.16	0.808	24.85	0.790	25.60	0.843	21.24	0.782	22.79	0.763

6.1.3 Details of Figure 1

We also present the supplementary information for Figure 1. Let $(\mathbf{y}_0^{(2)}, \dots, \mathbf{y}_{24}^{(2)})$ denote a sequence of noisy images with denaturation. For each $\mathbf{y}_t^{(2)}$, it is constructed from $\mathbf{x}_t^{(2)}$ of $\mathcal{D}_2^{\text{toy}}$ by Poisson-Gaussian noise with $(\lambda, \sigma) = (10, 10)$. For (1a) (resp. (1b)), we visualize $\mathbf{y}_0^{(2)}$ (resp. $\mathbf{y}_{12}^{(2)}$). As for (1e), it is the predicted image from our trained model of Section 6.1.2 by $(\mathbf{y}_0^{(2)}, \dots, \mathbf{y}_{24}^{(2)})$.

6.2 Expt.2: Performance Evaluation using MRI Image Dataset

6.2.1 Setting

Following [14], we employ time series MRI image dataset called ACDC [48]. According to [48], all the dataset contains gray-scaled images whose sizes are 192×192 each. Among 20 healthy patients in the dataset, we firstly pick the first five IDs (i.e., from ID 1 to ID 5), and for each ID, we use the first 25 images in ascending order of time. Following [47], we then add the Poisson-Gaussian noise with the hyperparameter values $(\lambda, \sigma) = (10, 50)$ to all the images independently; see an example for the noisy images in (2a) of Figure 2.

Regarding the performance comparison, we employ three state-of-the-art-methods: the non-deep-learning method called “BM3D” [1], the self-supervised single image denoising method called “Noise2Fast” (N2F) [28], and the self-supervised deformed image denoising method called “Deformed2Self” (D2S) [14]. We here explain detailed usage of the three existing methods employed in Expt.2. Let $\mathcal{D} = (\mathbf{y}_0, \dots, \mathbf{y}_t, \dots, \mathbf{y}_{T-1})$ denote a sequence of noisy denaturing images, where $t \in \mathbb{N} \cup \{0\}$ is the time index. Then, we consider the following settings:

- BM3D [1]: We apply the module [49] provided by the authors of [50] to the non-denatured noisy image \mathbf{y}_0 .
- Noise2Fast (N2F) [28]: We run the GitHub code of [51] using only \mathbf{y}_0 .
- Deformed2Self (D2S) [14]: We apply the GitHub code of [52] to \mathcal{D} .

6.2.2 Result and Discussion

Result The quantitative results are in Table 2. From the table, we can see that our method performs overall better than the three existing methods, and the second best performing method is D2S.

Discussion with Visualization Regarding visualization of the predicted images generated by our method, see Figure 2. For example, by zoom-in, we can observe that the prediction of (2k) is sufficiently denoised compared to (2i) and comparable to the clean counterpart (2l). Furthermore, by comparing (2j) and (2l) in terms of the remaining noise, we can see that our method performs better for the sub-image than D2S.

6.3 Expt.3: Performance Evaluation using Cryo-EM Image Dataset

6.3.1 Setting

We employ a multiframe file containing 16 Cryo-EM images of multiple particles from the dataset called EMPIAR-10028 [53]. Let us define the time series raw 16 Cryo-EM images by $(\mathbf{y}_0, \mathbf{y}_1, \dots, \mathbf{y}_t, \dots, \mathbf{y}_{15})$, where $t \in \mathbb{N}$ is the time index. According to [53], all the images are of size 4096×4096 , and are contaminated by noise. Since the original image size is too large for our computational resources to train our model, we firstly select two different small areas (both sizes are 192×192) containing single particle in \mathbf{y}_0 , using the average Cryo-EM image $\bar{\mathbf{x}} := \sum_{t=0}^{15} \mathbf{y}_t / 16$. The selected two areas in \mathbf{y}_0 are visualized as two yellow squared regions in (3a); see also zoom-in images for the two areas in (3c) and (3e). The corresponding sub images to (3a) in $\bar{\mathbf{x}}$ is visualized in (3b). For each Cryo-EM image in $\mathbf{y}_0, \dots, \mathbf{y}_{15}$, we clip two small square areas based on the coordinates of the two yellow squared areas in (3a) to make training datasets of DN2N. We denoise the two small areas of (3c) and (3e) by using our trained model and then conduct visual inspection to evaluate the predictions.

Remark 1. *An averaged image over raw Cryo-EM images is commonly used as a higher-resolution reference to the raw images, when reconstructing the 3D protein structures by RELION [11] or cryoSPARC [12]. The goal of Expt.3 is to check whether our method can be an efficient preprocessing technique before the averaging. If it is efficient, our method has a potential to enhance quality of the averaged image, leading more accurate 3D reconstruction.*

We additionally show the details of the experiments in the next paragraph.

Supplementary Information for Figure 3 We provide coordinates' information with (3a) in Figure 3. First, (3a) is a sub-image in the original Cryo-EM image at $t = 0$, i.e., \mathbf{y}_0 , whose size is 4096×4096 . Following the introduction of the coordinates in Section 6.1.1, the top-left, bottom-left, bottom-right, and top-right corners' coordinates of \mathbf{y}_0 are $(1, 1)$, $(1, 4096)$, $(4096, 4096)$, and $(4096, 1)$, respectively. We define the coordinates of the bottom-left, bottom-right, top-right, and top-left corners of the sub-image (3a) in \mathbf{y}_0 by A, B, C , and D , respectively. Moreover, we define the coordinates of the top-left corner point in the top-left (resp. bottom-right) yellow square of (3a)

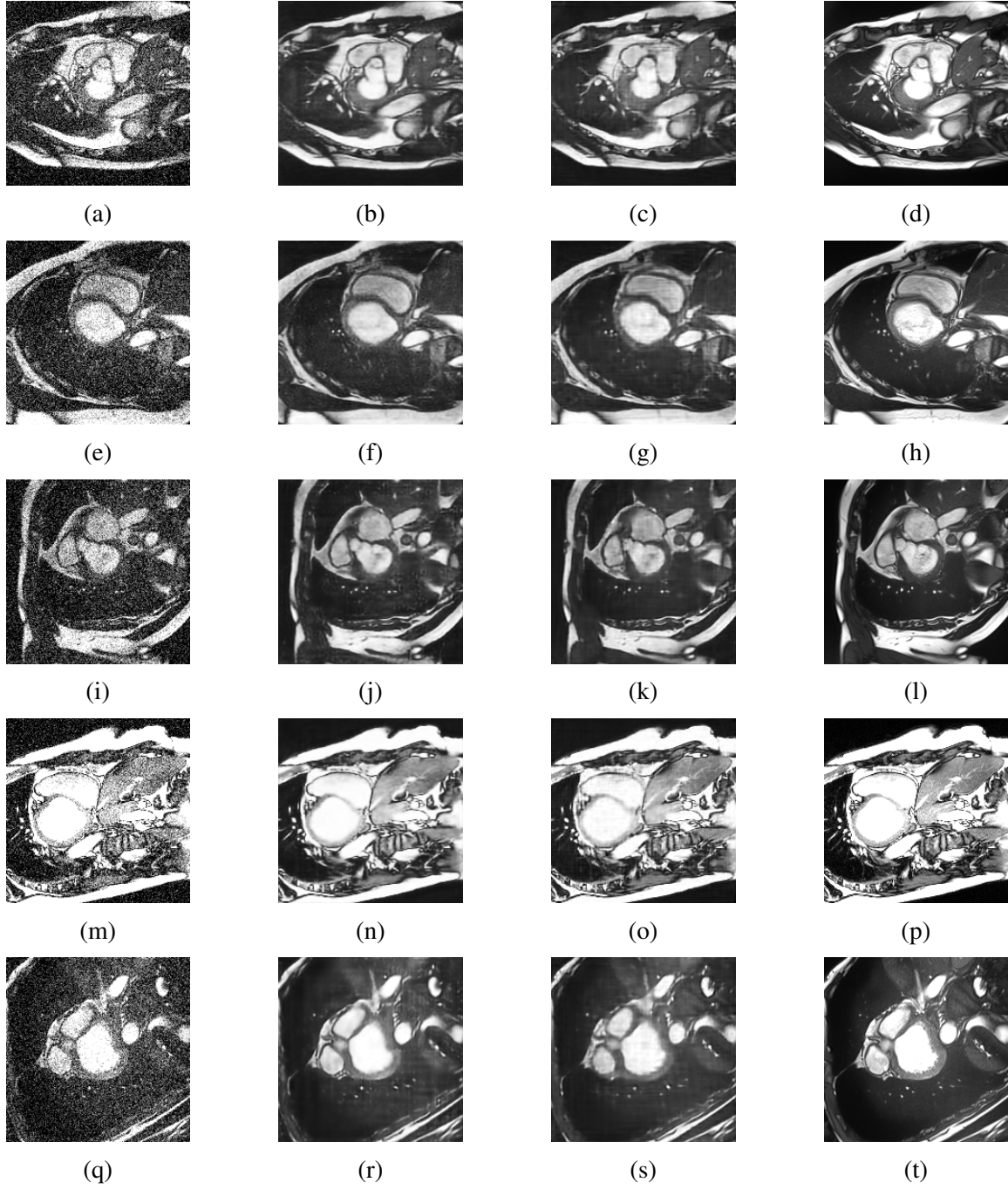


Figure 2: Visualization of predicted images by our method in Expt.2. The first, second, third, and fourth columns correspond to a noisy image at $t = 0$, predicted image by D2S, predicted image by our method DN2N, and clean image at $t = 0$, respectively. The first to fifth rows correspond to ID 1 to ID 5, respectively.

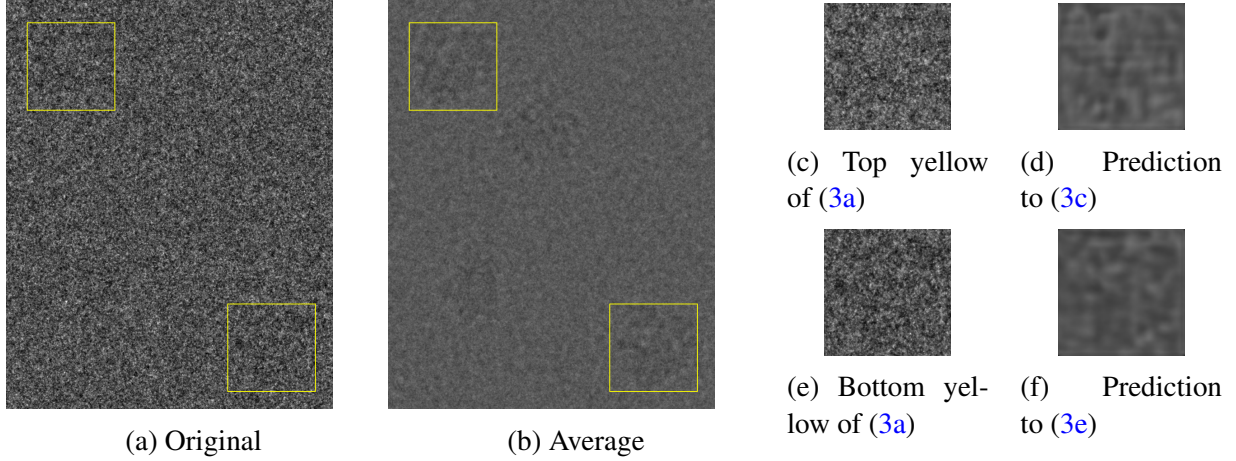


Figure 3: Visualized results of Expt.3: application of our method to two small yellow squared areas in (3a). (3a): Sub-image in a raw Cryo-EM image at $t = 0$. (3b): The corresponding sub-image to (3a) in the averaged Cryo-EM image. (3c) and (3e): The clipped two yellow squared areas from (3a) by `Fi Ji` [54]. (3d) and (3f): Predicted images by our method for (3c) and (3e), respectively. mildenhall2018burst

in y_0 by E (resp. F). In this case, $A = (593, 3836)$, $B = (1316, 3836)$, $C = (1316, 2925)$, $D = (593, 2925)$, $E = (641, 2981)$, and $F = (1085, 3605)$.

6.3.2 Result and Analysis

The results are presented in Figure 3. Let us treat the average image \bar{x} as a higher-resolution reference for y_0 ; see Remark 1. First, we can faintly see that each area surrounded by yellow squares in the average sub-image (3b) contains a circular particle, whereas we can see almost no particle in the same areas of (3a). Next, we can faintly see a circular-shaped particle in the prediction (3d) (resp. (3f)) and the particle is similar to one in the top-left (resp. bottom-right) yellow squared region of (3b). Further, the particles in (3d) and (3f) are relatively more visible than the counterparts in (3c) and (3e).

6.4 Implementation and Hyperparameter Tuning

We implement the algorithms with `PyTorch` [55]. For the architecture, we employ the model used in [3], which is based on the architecture called U-Net [56]. Here, since our algorithm requires the time variable, we create additional one-channel tensor directly using `PyTorch` [55], whose shape is $W \times H$ and each entry is equal to the value of the time variable, and we add it to each C -channel training image to produce a $(C + 1)$ -channel image of shape $W \times H$. Note that following [3], we divide the loss function by the number of pixels in each image input to the networks.

In our method, there are the following main hyperparameters: $\tilde{\sigma}$, μ , L , and K . The hyperparameter $\tilde{\sigma}$ represents the standard deviation of the multivariate zero-mean normal distribution, from which the auxiliary noise ε in (5) is sampled. The hyperparameter μ is used to define $\hat{\mathcal{L}}_T$ in

Table 3: Results of prediction performance by DN2N with the different hyperparameter values $(\tilde{\sigma}, \mu)$ on the ACDC dataset defined in Expt.2, while fixing (L, K) to $(2, 100)$. Note that the result for the selection $(\tilde{\sigma}, \mu) = (75, 10)$ is shown in the last row of Table 2.

$\tilde{\sigma}$	μ	ID 1		ID 2		ID 3		ID 4		ID 5	
		PSNR \uparrow	SSIM \uparrow	PSNR	SSIM	PSNR	SSIM	PSNR	SSIM	PSNR	SSIM
50	0.1	23.15	0.789	24.62	0.767	24.92	0.817	20.78	0.768	22.95	0.763
	1	23.01	0.795	24.28	0.763	24.82	0.825	21.26	0.778	22.79	0.744
	10	23.06	0.800	24.54	0.782	25.42	0.830	21.36	0.785	22.90	0.779
	100	22.87	0.802	24.89	0.801	25.54	0.840	21.31	0.782	22.90	0.773
75	0.1	23.10	0.792	24.34	0.780	25.51	0.838	21.02	0.775	22.85	0.766
	1	23.16	0.796	24.53	0.771	25.30	0.827	20.99	0.768	22.99	0.752
	100	22.73	0.802	24.21	0.797	25.39	0.842	21.25	0.779	22.79	0.770
	100	22.52	0.800	24.84	0.798	25.26	0.841	20.74	0.771	22.68	0.769

Section 5. The quantities L and K respectively denote the number of transformations in (5) and the number of reconstructed images used for the prediction \hat{x}_0 in (6). From the hyperparameter tuning results shown in Table 3, we set $(\tilde{\sigma}, \mu, L, K)$ to $(50, 100, 2, 100)$ in Expt.1, to $(75, 10, 2, 100)$ in Expt.2, and to $(75, 10, 2, 100)$ in Expt.3. The predicting performance of DN2N is robust against change of $(\tilde{\sigma}, \mu)$; see Table 3. We use the optimizer called Adam [57], where we set the learning rate to 0.0001. Moreover, we set the number of epochs for training model to 1000 (resp. 900) in Expt.1 and Expt.2 (resp. Expt.3).

We note that the quantities (M, N) of Section 5 are $(1, 24)$ (resp. $(1, 15)$) in Expt.1 and Expt.2 (resp. Expt.3), where the time τ defined in Section 2.1 is uniformly distributed in all the three experiments, and we sample the image corresponding to each τ drawn according to the procedure.

7 Conclusion

We theoretically analyze the prediction performance of a self-supervised denoising method on noisy images with denaturation. Based on the analytical result in Theorem 1, we design DN2N. In our numerical experiments, we observe that the performance of DN2N on the synthetic dataset is consistent with the analytical result. Further, DN2N empirically performs well for both MRI and Cryo-EM image datasets.

We conclude this paper by presenting two interesting directions remained. We firstly point out that relaxing Assumption 1 to more general assumptions is crucial for applications. In addition, constructing more efficient ways to reduce the influence from the hardness of denaturation levels is also important to make full use of denatured images.

Acknowledgments

This work was supported by the FOCUS Establishing Supercomputing Center of Excellence project; MEXT as “Program for Promoting Researches on the Supercomputer Fugaku” (Simulation- and AI-driven next-generation medicine and drug discovery based on “Fugaku”, JPMXP1020230120). This work used computational resources of the supercomputer Fugaku provided by RIKEN Center for Computational Science through the HPCI System Research Projects (Project IDs: hp220078, hp230102, hp230216, hp240109, hp240211,ra000018); the supercomputer system at the information initiative center, Hokkaido University, Sapporo, Japan through the HPCI System Research Projects (Project IDs: hp220078, hp230102). Computational resources of AI Bridging Cloud Infrastructure (ABCI) provided by the National Institute of Advanced Industrial Science and Technology (AIST) was also used. We would like to thank Yasushi Okuno, Akira Nakagawa, and Takashi Kato for their feedback on the draft.

A Proofs

In this section, we provide all the proofs omitted in the main paper.

A.1 Proof of Proposition 1

Proof. In the first step, we derive the optimal solution of the least-squares problem. We follow a similar way to Section 2.4 in [35] for solving the least-squares problem. Note that

$$\mathbb{E}_{\mathbf{y},\tau}[\|\mathbf{f}(\mathbf{y}_0, \tau) - \mathbf{y}_\tau\|_2^2 | \mathbf{x}_0] = \mathbb{E}_{\mathbf{y}_0, \tau}[\mathbb{E}_{\mathbf{y}_\tau}[\|\mathbf{f}(\mathbf{y}_0, \tau) - \mathbf{y}_\tau\|_2^2 | \tau, \mathbf{y}_0] | \mathbf{x}_0].$$

For a fixed τ , note that \mathbf{x}_0 has been also fixed. Then, it holds that

$$\begin{aligned} & \mathbb{E}_{\mathbf{y}_\tau}[\|\mathbf{f}(\mathbf{y}_0, \tau) - \mathbf{y}_\tau\|_2^2 | \tau, \mathbf{y}_0] \\ &= \sum_{i=1}^d \mathbb{E}_{\mathbf{y}_\tau}[f_i^2(\mathbf{y}_0, \tau) - 2\mathbf{y}_{\tau,i}f(\mathbf{y}_0, \tau)_i + \mathbf{y}_{\tau,i}^2 | \tau, \mathbf{y}_0] \\ &= \sum_{i=1}^d \{ (f_i(\mathbf{y}_0, \tau) - \mathbb{E}_{\mathbf{y}_\tau}[\mathbf{y}_{\tau,i} | \tau, \mathbf{y}_0])^2 - (\mathbb{E}_{\mathbf{y}_\tau}[\mathbf{y}_{\tau,i} | \tau, \mathbf{y}_0])^2 + \mathbb{E}_{\mathbf{y}_\tau}[\mathbf{y}_{\tau,i}^2 | \tau, \mathbf{y}_0] \}, \end{aligned}$$

where $f_i(\mathbf{y}_0, \tau)$ and $\mathbf{y}_{\tau,i}$ denote the i -th index of the vectors, respectively. This indicates that $f^*(\mathbf{y}_0, \tau) = \mathbb{E}_{\mathbf{y}_\tau}[\mathbf{y}_\tau | \tau, \mathbf{y}_0]$ almost surely.

Now, we consider to fix $\mathbf{y}_0 \in \mathbb{R}^d$ for convenience. For $t > 0$, letting $t \downarrow 0$,

$$\lim_{t \downarrow 0} f^*(\mathbf{y}_0, t) = \lim_{t \downarrow 0} \phi_t(\mathbf{x}_0) = \mathbf{x}_0,$$

where we use in the first equality that $\mathbb{E}_{\mathbf{y}_t}[\mathbf{y}_t | \mathbf{y}_0] = \phi_t(\mathbf{x}_0)$ from the conditions (A) and (C) in Assumption 1, and in the second one, the condition (B) in Assumption 1. Here, from the assumption, it holds that $\lim_{t \downarrow 0} f^*(\mathbf{y}_0, t) = f^*(\mathbf{y}_0, 0)$. Therefore, $f^*(\mathbf{y}_0, 0) = \mathbf{x}_0$ holds almost every \mathbf{y}_0 with its probability measure. This implies that $\mathbb{E}_{\mathbf{y}_0}[f^*(\mathbf{y}_0, 0) | \mathbf{x}_0] = \mathbf{x}_0$, as claimed. \square

A.2 Proof of Theorem 1

We note that the following fact holds.

Lemma 1. *Suppose that the conditions in the statement of Theorem 1 hold. Let $V = \{\mathbf{v} \in \mathbb{R}^d \mid \|\mathbf{v}\|_2 \leq B_2\}$. Then for any $f \in \mathcal{F}$, it holds that*

$$\sup_{\mathbf{u} \in U, \mathbf{v} \in V, t \in (0,1]} \|f(\mathbf{u}, t) - \mathbf{v}\|_2^2 \leq L^2(B_1^2 + 1) + B_2^2.$$

Proof. First note that

$$\sup_{\mathbf{u} \in U, \mathbf{v} \in V, t \in (0,1]} \|f(\mathbf{u}, t) - \mathbf{v}\|_2^2 \leq \left(\sup_{\mathbf{u} \in U, t \in (0,1]} \|f(\mathbf{u}, t)\|_2 + \sup_{\mathbf{v} \in V} \|\mathbf{v}\|_2 \right)^2.$$

The second term in the upper bound is further bounded by B_2 from the condition on V . For the first part, notice that $f(\mathbf{0}, 0) = 0$ holds and f is L -Lipschitz, we have

$$\sup_{\mathbf{u} \in U, t \in (0,1]} \|f(\mathbf{u}, t)\|_2 \leq L\sqrt{\|\mathbf{u}\|_2^2 + |t|^2} \leq L\sqrt{B_1^2 + 1}.$$

Hence, we obtain

$$\sup_{\mathbf{u} \in U, \mathbf{v} \in V, t \in (0,1]} \|f(\mathbf{u}, t) - \mathbf{v}\|_2^2 \leq \left(L\sqrt{B_1^2 + 1} + B_2 \right)^2,$$

which shows the claim. \square

Following [38, Definition 3.2], we define a variant of *Rademacher complexity* [37] as

$$\mathcal{R}_j(\mathcal{F}) = \mathbb{E}_{\tau, \sigma} \left[\sup_{f \in \mathcal{F}} \frac{1}{N} \sum_{i=1}^N \sigma_i \|f(\mathbf{y}_{0,j}, \tau_i) - \mathbf{y}_{\tau_i,j}\|_2^2 \right],$$

where $\{\sigma_i\}$ are i.i.d. random variables such that $\sigma_i = +1$ holds with probability 1/2 and $\sigma_i = -1$ holds with probability 1/2, and the expectation is taken for all random variables except \mathbf{y} . To prove Theorem 1, we need the following inequality, whose proof is based on [38, Theorem 3.3].

Lemma 2. *In the setting described in the statement of Theorem 1, with probability at least $1 - 2\delta$ where $\delta \geq 0$, it holds that*

$$\begin{aligned} & \frac{1}{MN} \sum_{j=1}^M \sum_{i=1}^N \|f(\mathbf{y}_{0,j}, \tau_i) - \mathbf{y}_{\tau_i,j}\|_2^2 \\ & \leq \mathbb{E} [\|f(\mathbf{y}_0, \tau_i) - \mathbf{y}_{\tau_i}\|_2^2] + 2 \frac{1}{M} \sum_{j=1}^M \mathcal{R}_j(\mathcal{F}) \\ & \quad + \sqrt{\frac{2B^2 \log(M/\delta)}{N}} + \sqrt{\frac{2B^2 \log(1/\delta)}{M}}. \end{aligned}$$

The proof of Lemma 2 can be found in Appendix A.3.

In the proof of Theorem 1, we upper bound the following quantity.

Lemma 3. *Suppose that the setting in Theorem 1 holds. Then, there exists a constant $C > 0$ such that we have*

$$\mathbb{E}_{\tau, \sigma} \left[\sup_{f \in \mathcal{F}} \frac{1}{N} \sum_{i=1}^N \sigma_i \|f(\mathbf{y}_{0,j}, \tau_i)\|_2 \right] \leq C \frac{1}{\sqrt{N}}.$$

The proof of Lemma 3 is differed to A.4. We also need the following lemma.

Lemma 4. *In the setting of Theorem 1, there is a positive constant C such that we have*

$$\mathbb{E}_{\tau, \sigma} \left[\sup_{f \in \mathcal{F}} \frac{1}{N} \sum_{i=1}^N \sigma_i \langle f(\mathbf{y}_{0,j}, \tau_i), \mathbf{y}_{\tau_i, j} \rangle_2 \right] \leq C \frac{1}{\sqrt{N}}.$$

The proof of Lemma 4 can be found in Appendix A.4.

Proof of Theorem 1. We first remark that throughout this proof, the clean image $\mathbf{x}_0 \in \mathbb{R}^d$ is fixed. Using the triangle inequality, it holds that

$$\begin{aligned} & \|\hat{\mathbf{x}}_0 - \mathbf{x}_0\|_2^2 \\ &= \left\| \hat{\mathbf{x}}_0 - \frac{1}{MN} \sum_{j=1}^M \sum_{i=1}^N \hat{f}(\mathbf{y}_{0,j}, \tau_i) + \frac{1}{MN} \sum_{j=1}^M \sum_{i=1}^N \hat{f}(\mathbf{y}_{0,j}, \tau_i) - \mathbf{x}_0 \right\|_2^2 \\ &\leq 2 \left\| \frac{1}{M} \sum_{j=1}^M \hat{f}(\mathbf{y}_{0,j}, 0) - \frac{1}{MN} \sum_{j=1}^M \sum_{i=1}^N \hat{f}(\mathbf{y}_{0,j}, \tau_i) \right\|_2^2 \\ &\quad + 2 \left\| \frac{1}{MN} \sum_{j=1}^M \sum_{i=1}^N \hat{f}(\mathbf{y}_{0,j}, \tau_i) - \mathbf{x}_0 \right\|_2^2. \end{aligned} \tag{9}$$

The first term in (9) is upper bounded as

$$\begin{aligned} & \left\| \frac{1}{M} \sum_{j=1}^M \hat{f}(\mathbf{y}_{0,j}, 0) - \frac{1}{MN} \sum_{j=1}^M \sum_{i=1}^N \hat{f}(\mathbf{y}_{0,j}, \tau_i) \right\|_2^2 \\ &\leq \frac{1}{MN} \sum_{j=1}^M \sum_{i=1}^N \left\| \hat{f}(\mathbf{y}_{0,j}, 0) - \hat{f}(\mathbf{y}_{0,j}, \tau_i) \right\|_2^2 \\ &\leq L^2 \cdot \frac{1}{N} \sum_{i=1}^N \tau_i^2, \end{aligned} \tag{10}$$

where in the first inequality we use the triangle inequality, and in the second line we utilize the Lipschitz continuity of \hat{f} as assumed in the statement. Here $\tau_i(\omega) \in (0, 1]$ for every $\omega \in \Omega$ from

the definition. By Hoeffding's inequality (see e.g., Theorem D.2 in [38]), for the mean $\frac{1}{N} \sum_{i=1}^N \tau_i^2$ we have with probability at least $1 - \delta$,

$$\frac{1}{N} \sum_{i=1}^N \tau_i^2 \leq \mathbb{E}[\tau^2] + \sqrt{\frac{\log(1/\delta)}{2N}}. \quad (11)$$

By (10) and (11), with probability at least $1 - \delta$ we have

$$\left\| \frac{1}{M} \sum_{j=1}^M \hat{f}(\mathbf{y}_{0,j}, 0) - \frac{1}{MN} \sum_{j=1}^M \sum_{i=1}^N \hat{f}(\mathbf{y}_{0,j}, \tau_i) \right\|_2^2 \leq L^2 \cdot \left(\mathbb{E}[\tau^2] + \sqrt{\frac{\log(1/\delta)}{2N}} \right). \quad (12)$$

The second term in (9) is evaluated as follows:

$$\begin{aligned} & \left\| \frac{1}{MN} \sum_{j=1}^M \sum_{i=1}^N \hat{f}(\mathbf{y}_{0,j}, \tau_i) - \mathbf{x}_0 \right\|_2^2 \\ & \leq 2 \left\| \frac{1}{MN} \sum_{j=1}^M \sum_{i=1}^N \hat{f}(\mathbf{y}_{0,j}, \tau_i) - \frac{1}{MN} \sum_{j=1}^M \sum_{i=1}^N \mathbf{y}_{\tau_i,j} \right\|_2^2 \\ & \quad + 2 \left\| \frac{1}{MN} \sum_{j=1}^M \sum_{i=1}^N \mathbf{y}_{\tau_i,j} - \mathbf{x}_0 \right\|_2^2 \\ & \leq \frac{2}{MN} \sum_{j=1}^M \sum_{i=1}^N \left\| \hat{f}(\mathbf{y}_{0,j}, \tau_i) - \mathbf{y}_{\tau_i,j} \right\|_2^2 + 2 \left\| \frac{1}{MN} \sum_{j=1}^M \sum_{i=1}^N \mathbf{y}_{\tau_i,j} - \mathbf{x}_0 \right\|_2^2. \end{aligned} \quad (13)$$

Let $B = \left(L\sqrt{B_1^2 + 1} + B_2 \right)^2$. By Lemma 1 and Lemma 2, the following inequality holds with probability at least $1 - 2\delta$

$$\begin{aligned} & \frac{1}{MN} \sum_{j=1}^M \sum_{i=1}^N \|f^*(\mathbf{y}_{0,j}, \tau_i) - \mathbf{y}_{\tau_i,j}\|_2^2 \\ & \leq \mathbb{E}[\|f^*(\mathbf{y}_0, \tau) - \mathbf{y}_\tau\|_2^2] + \frac{2}{M} \sum_{j=1}^M \mathcal{R}_j(\mathcal{F}) + \sqrt{\frac{B^2 \log(M/\delta)}{2N}} + \sqrt{\frac{2B^2 \log(1/\delta)}{2M}}. \end{aligned} \quad (14)$$

Since \hat{f} is the empirical risk minimizer, (14) yields the following inequality that holds with probability at least $1 - 2\delta$:

$$\begin{aligned} & \frac{1}{MN} \sum_{j=1}^M \sum_{i=1}^N \left\| \hat{f}(\mathbf{y}_{0,j}, \tau_i) - \mathbf{y}_{\tau_i,j} \right\|_2^2 \\ & \leq \mathbb{E}[\|f^*(\mathbf{y}_0, \tau) - \mathbf{y}_\tau\|_2^2] + \frac{2}{M} \sum_{j=1}^M \mathcal{R}_j(\mathcal{F}) + \sqrt{\frac{B^2 \log(M/\delta)}{2N}} + \sqrt{\frac{B^2 \log(1/\delta)}{2M}}. \end{aligned} \quad (15)$$

Here we rearrange $\mathcal{R}(\mathcal{F})$ to obtain a bound,

$$\begin{aligned}
& \mathcal{R}_j(\mathcal{F}) \\
&= \mathbb{E}_{\tau, \sigma} \left[\sup_{f \in \mathcal{F}} \frac{1}{N} \sum_{i=1}^N \sigma_i \left(\|f(\mathbf{y}_{0,j}, \tau_i)\|_2^2 - 2\langle f(\mathbf{y}_{0,j}, \tau_i), \mathbf{y}_{\tau_i} \rangle_2 + \|\mathbf{y}_{\tau_i}\|_2^2 \right) \right] \\
&\leq \mathbb{E}_{\tau, \sigma} \left[\sup_{f \in \mathcal{F}} \frac{1}{N} \sum_{i=1}^N \sigma_i \left(\|f(\mathbf{y}_{0,j}, \tau_i)\|_2^2 + \|\mathbf{y}_{\tau_i}\|_2^2 \right) + 2 \sup_{f \in \mathcal{F}} \frac{1}{N} \sum_{i=1}^N -\sigma_i \langle f(\mathbf{y}_{0,j}, \tau_i), \mathbf{y}_{\tau_i} \rangle_2 \right] \quad (16) \\
&= \mathbb{E}_{\tau, \sigma} \left[\sup_{f \in \mathcal{F}} \frac{1}{N} \sum_{i=1}^N \sigma_i \left(\|f(\mathbf{y}_{0,j}, \tau_i)\|_2^2 + \|\mathbf{y}_{\tau_i}\|_2^2 \right) + 2 \sup_{f \in \mathcal{F}} \frac{1}{N} \sum_{i=1}^N \sigma_i \langle f(\mathbf{y}_{0,j}, \tau_i), \mathbf{y}_{\tau_i} \rangle_2 \right],
\end{aligned}$$

where we note that in (16) we utilize the obvious fact that σ_i and $-\sigma_i$ follow the same distribution. Since $\mathbb{E}_{\sigma_i}[\sigma_i] = 0$ from the definition of σ_i , we have

$$\begin{aligned}
& \mathbb{E}_{\tau, \sigma} \left[\sup_{f \in \mathcal{F}} \frac{1}{N} \sum_{i=1}^N \sigma_i \left(\|f(\mathbf{y}_{0,j}, \tau_i)\|_2^2 + \|\mathbf{y}_{\tau_i}\|_2^2 \right) \right] \\
&\leq \mathbb{E}_{\tau, \sigma} \left[\sup_{f \in \mathcal{F}} \frac{1}{N} \sum_{i=1}^N \sigma_i \|f(\mathbf{y}_{0,j}, \tau_i)\|_2^2 \right]. \quad (17)
\end{aligned}$$

Then, by Talagland's contraction inequality (see e.g., Lemma 5.7 in [38]) to the first term in the right-hand-side of (17), it holds that

$$\begin{aligned}
& \mathbb{E}_{\tau, \sigma} \left[\sup_{f \in \mathcal{F}} \frac{1}{N} \sum_{i=1}^N \sigma_i \|f(\mathbf{y}_{0,j}, \tau_i)\|_2^2 \right] \\
&\leq 2L\sqrt{B_1^2 + 1} \cdot \mathbb{E}_{\tau, \sigma} \left[\sup_{f \in \mathcal{F}} \frac{1}{N} \sum_{i=1}^N \sigma_i \|f(\mathbf{y}_{0,j}, \tau_i)\|_2 \right]. \quad (18)
\end{aligned}$$

By Lemma 3, Lemma 4, (13), (15), (16), (17), and (18), with probability at least $1 - 2\delta$ we have

$$\begin{aligned}
& \frac{1}{MN} \sum_{j=1}^M \sum_{i=1}^N \left\| \hat{f}(\mathbf{y}_{0,j}, \tau_i) - \mathbf{y}_{\tau_i,j} \right\|_2^2 \\
&\leq \mathbb{E}[\|f^*(\mathbf{y}_0, \tau) - \mathbf{y}_\tau\|_2^2] + 4C(L\sqrt{B_1^2 + 1} + 1) \frac{1}{\sqrt{N}} \\
&\quad + 3\sqrt{\frac{B^2 \log(M/\delta)}{2N}} + \sqrt{\frac{B^2 \log(1/\delta)}{2M}}. \quad (19)
\end{aligned}$$

Next, we upper bound the second term in (13) as

$$\begin{aligned}
& \left\| \frac{1}{MN} \sum_{j=1}^M \sum_{i=1}^N \mathbf{y}_{\tau_i, j} - \mathbf{x}_0 \right\|_2^2 \\
& \leq 2 \left\| \frac{1}{MN} \sum_{j=1}^M \sum_{i=1}^N \mathbf{y}_{\tau_i, j} - \mathbb{E}[\mathbf{y}_\tau | \mathbf{x}_0] \right\|_2^2 + \frac{2}{MN} \sum_{j=1}^M \sum_{i=1}^N \|\mathbb{E}[\mathbf{y}_{\tau_i, j} | \mathbf{x}_0] - \mathbf{x}_0\|_2^2 \\
& = 2 \left\| \frac{1}{MN} \sum_{j=1}^M \sum_{i=1}^N \mathbf{y}_{\tau_i, j} - \mathbb{E}[\mathbf{y}_\tau | \mathbf{x}_0] \right\|_2^2 + \frac{2}{MN} \sum_{j=1}^M \sum_{i=1}^N \|\mathbb{E}_{\tau_i}[\phi_{\tau_i}(\mathbf{x}_0)] - \mathbf{x}_0\|_2^2 \quad (20)
\end{aligned}$$

$$= 2 \left\| \frac{1}{MN} \sum_{j=1}^M \sum_{i=1}^N \mathbf{y}_{\tau_i, j} - \mathbb{E}[\mathbf{y}_\tau | \mathbf{x}_0] \right\|_2^2 + 2 \|\mathbb{E}_\tau[\phi_\tau(\mathbf{x}_0)] - \mathbf{x}_0\|_2^2 \quad (21)$$

$$\leq 2 \left\| \frac{1}{MN} \sum_{j=1}^M \sum_{i=1}^N \mathbf{y}_{\tau_i, j} - \mathbb{E}[\mathbf{y}_\tau | \mathbf{x}_0] \right\|_1^2 + 2 \|\mathbb{E}_\tau[\phi_\tau(\mathbf{x}_0)] - \mathbf{x}_0\|_2^2, \quad (22)$$

where in (20) we use the condition (A) in Assumption 1. Here we note the condition in the statement that $\|\mathbf{y}_{\tau_i, j}\|_2 \leq B_2$ holds almost surely. Here note that by Jensen's inequality

$$\left| \frac{1}{MN} \sum_{j=1}^M \sum_{i=1}^N \mathbf{y}_{\tau_i, j, k} - \mathbb{E}[\mathbf{y}_{\tau, k} | \mathbf{x}_0] \right| \leq \frac{1}{M} \sum_{j=1}^M \left| \frac{1}{N} \sum_{i=1}^N \mathbf{y}_{\tau_i, j, k} - \mathbb{E}[\mathbf{y}_{\tau, j, k} | \mathbf{x}_0] \right|. \quad (23)$$

By Hoeffding's inequality (see e.g., Theorem D.2 in [38]), with probability at least $1 - 2(Md)^{-1}\delta$ it holds that

$$\left| \frac{1}{N} \sum_{i=1}^N \mathbf{y}_{\tau_i, j, k} - \mathbb{E}[\mathbf{y}_{\tau, j, k} | \mathbf{x}_0] \right| \leq \sqrt{\frac{B_2^2 \log(2Md/\delta)}{2N}}. \quad (24)$$

By (23) and (24), with probability at least $1 - 2\delta$ it holds that

$$\left\| \frac{1}{MN} \sum_{j=1}^M \sum_{i=1}^N \mathbf{y}_{\tau_i, j} - \mathbb{E}[\mathbf{y}_\tau | \mathbf{x}_0] \right\|_1^2 \leq \frac{d^2 B_2^2 \log(2Md/\delta)}{2N}. \quad (25)$$

Finally, combining (9), (12), (13), (19), (22), and (25), with probability at least $1 - 4\delta$, we have

$$\begin{aligned}
\|\hat{\mathbf{x}}_0 - \mathbf{x}_0\|_2^2 & \leq 2L^2 \mathbb{E}[\tau^2] + 2\mathbb{E}[\|f^*(\mathbf{y}_0, \tau) - \mathbf{y}_\tau\|_2^2] + 2\|\mathbb{E}_\tau[\phi_\tau(\mathbf{x}_0)] - \mathbf{x}_0\|_2^2 \\
& \quad + 2L^2 \sqrt{\frac{\log(1/\delta)}{2N}} + 4C(L\sqrt{B_1^2 + 1} + 1) \frac{1}{\sqrt{N}} \\
& \quad + 6\sqrt{\frac{B^2 \log(M/\delta)}{2N}} + 2\sqrt{\frac{B^2 \log(1/\delta)}{2M}} + \frac{d^2 B_2^2 \log(2Md/\delta)}{2N},
\end{aligned}$$

which shows the claim, and the proof is completed. \square

A.3 Proof of Lemma 2

Proof of Lemma 2. We first focus on each of the components in the decomposition

$$\frac{1}{MN} \sum_{j=1}^M \sum_{i=1}^N \|f(\mathbf{y}_{0,j}, \tau_i) - \mathbf{y}_{\tau_i,j}\|_2^2 = \frac{1}{M} \sum_{j=1}^M \left(\frac{1}{N} \sum_{i=1}^N \|f(\mathbf{y}_{0,j}, \tau_i) - \mathbf{y}_{\tau_i,j}\|_2^2 \right). \quad (26)$$

In the following, we treat $\mathbf{y}_{\tau_i,j}$ as a functional of τ_i , namely we fix the randomness of $\mathbf{y}_{t,j}$ by considering a realization of it. Here to avoid any confusion, we write $\mathbf{y}_j(\tau_i)$ instead to express that it is a functional. Then, the sum $N^{-1} \sum_{i=1}^N \|f(\mathbf{y}_{0,j}, \tau_i) - \mathbf{y}_{\tau_i,j}\|_2^2$ is a mean of the function $\|f(\mathbf{y}_0, \tau) - \mathbf{y}_\tau\|_2^2$ with i.i.d. random variables (τ_1, \dots, τ_N) . Thus, by Theorem 3.3 in [38], with probability at least $1 - \delta/M$ we have

$$\begin{aligned} & \frac{1}{N} \sum_{i=1}^N \|f(\mathbf{y}_{0,j}, \tau_i) - \mathbf{y}_j(\tau_i)\|_2^2 \\ & \leq \mathbb{E}_\tau [\|f(\mathbf{y}_{0,j}, \tau_i) - \mathbf{y}_j(\tau_i)\|_2^2] + 2\mathcal{R}_j(\mathcal{F}) + \sqrt{\frac{B^2 \log(M/\delta)}{2N}}. \end{aligned} \quad (27)$$

Since (27) holds for every $j \in \{1, \dots, M\}$, by taking the union bound, with probability at least $1 - \delta$ we have

$$\begin{aligned} & \frac{1}{MN} \sum_{j=1}^M \sum_{i=1}^N \|f(\mathbf{y}_{0,i}, \tau_i) - \mathbf{y}_j(\tau_i)\|_2^2 \\ & \leq \frac{1}{M} \sum_{j=1}^M \mathbb{E}_\tau [\|f(\mathbf{y}_{0,j}, \tau_i) - \mathbf{y}_j(\tau_i)\|_2^2] + \frac{2}{M} \sum_{j=1}^M \mathcal{R}_j(\mathcal{F}) + \sqrt{\frac{B^2 \log(M/\delta)}{2N}}. \end{aligned} \quad (28)$$

The equation (28) holds for any possible functional \mathbf{y}_j in this problem setting. By Hoeffding's inequality (see e.g., Theorem D.2 in [38]), with probability at least $1 - \delta$ it holds that

$$\begin{aligned} & \frac{1}{M} \sum_{j=1}^M \mathbb{E}_\tau [\|f(\mathbf{y}_{0,j}, \tau_i) - \mathbf{y}_j(\tau_i)\|_2^2] \\ & \leq \mathbb{E}_{\mathbf{y}, \tau} [\|f(\mathbf{y}_{0,j}, \tau_i) - \mathbf{y}_j(\tau_i)\|_2^2] + \sqrt{\frac{B^2 \log(1/\delta)}{2M}}. \end{aligned} \quad (29)$$

Combining (28) and (29), we obtain the claim. \square

A.4 Proofs of Lemma 3 and Lemma 4

The proof of Lemma 3 uses the following useful facts. Let $N_0 \in \mathbb{N}$ be an arbitrary integer, and let \mathcal{S} be an arbitrary measurable space. Let r_1, \dots, r_{N_0} be i.i.d. \mathcal{S} -valued random variables

drawn from some probability distribution, and let \mathcal{G} be a set of real-valued functions on \mathcal{S} . In [38, Definition 3.1], a version of *empirical Rademacher complexity* [37] is defined as

$$\widehat{\mathcal{R}}(\mathcal{G}) := \mathbb{E}_\sigma \left[\sup_{g \in \mathcal{G}} \frac{1}{N_0} \sum_{i=1}^{N_0} \sigma_i g(r_i) \right]. \quad (30)$$

Denote $\|g\|_{N_0}^2 = \frac{1}{N_0} \sum_{i=1}^{N_0} g^2(r_i)$. Also, $\mathcal{N}(\mathcal{G}, u, \|\cdot\|_{N_0})$ denotes the standard covering number of \mathcal{G} with ball coverings of radius u in the norm $\|\cdot\|_{N_0}$ (see e.g., Definition 4.2.2 in [39] for covering numbers).

It is shown by Theorem 18 in [36] that the following fact holds:

Lemma 5 (Special case of Theorem 18 in [36]). *Let $\mathcal{S} = [0, 1]$, and let ρ be the standard Euclidean distance in \mathcal{S} . Let $\tilde{\mathcal{G}}$ be a set of real-valued functions on \mathcal{S} such that every element is 1-Lipschitz with respect to the metric ρ . Then, there exists a constant $C > 0$ independent of N_0 such that it holds that*

$$\widehat{\mathcal{R}}(\tilde{\mathcal{G}}) \leq C \inf_{c>0} \left\{ c + \frac{1}{\sqrt{N_0}} \int_{c/4}^2 \sqrt{\mathcal{N}(\mathcal{S}, u/2, \rho) + \log u^{-1}} du \right\}.$$

Note that the above fact is a special case of Theorem 18 in [36].

Using the above fact, we now prove Lemma 3 and Lemma 4.

Proof of Lemma 3. Define the function class $\mathcal{G} = \{g(t) = \|f(\mathbf{y}_{0,j}, t)\|_2 \mid f \in \mathcal{F}\}$. We rescale every function g in \mathcal{G} to define

$$\tilde{\mathcal{G}} = \{\tilde{g}(t) = L^{-1}d^{-1}g(t) \mid g \in \mathcal{G}\}.$$

where $\mathbf{u} \in U$, and $t \in [0, 1]$. Denote $f = (f_1, \dots, f_d)$ for convenience. Here, we notice that for any $\tilde{g} \in \tilde{\mathcal{G}}$,

$$\begin{aligned} |\tilde{g}(t) - \tilde{g}(t')| &\leq L^{-1}d^{-1} \|f(\mathbf{y}_{0,j}, t) - f(\mathbf{y}_{0,j}, t')\|_2 \\ &\leq |t - t'|, \end{aligned} \quad (31)$$

where in (31) we use the L -Lipschitzness of f . Therefore, by Lemma 5 due to [36], there exists some constant $C > 0$ independent of N such that

$$\widehat{\mathcal{R}}(\mathcal{G}) \leq LC \inf_{c>0} \left\{ c + \frac{1}{\sqrt{N}} \int_{c/4}^2 \sqrt{\mathcal{N}([0, 1], u/2, \|\cdot\|_2) + \log u^{-1}} du \right\}. \quad (32)$$

In the remaining part, we follow a similar way to Example 4 in [36]. By Corollary 4.2.13 in [39], for the quantity $\mathcal{N}([0, 1], u/2, \|\cdot\|_2)$ there exists a constant $C > 0$ independent of u such that

$$\mathcal{N}([0, 1], u/2, \|\cdot\|_2) \leq \frac{C}{u}. \quad (33)$$

We can bound the following integral:

$$\begin{aligned} \int_{c/4}^2 \sqrt{\frac{1}{u} + \log\left(\frac{1}{u}\right)} du &\leq \int_{c/4}^2 \sqrt{\frac{1}{u}} du + \int_{c/4}^2 \sqrt{\log\left(\frac{1}{u}\right)} du \\ &\lesssim 1, \end{aligned} \quad (34)$$

where the notation $a_1 \lesssim a_2$ ($a_1, a_2 \in \mathbb{R}$) means that $a_1 \leq C a_2$ for some constant $C > 0$. Combining (32), (33), (34), we have

$$\widehat{\mathcal{R}}(\mathcal{G}) \lesssim \inf_{c>0} \left\{ c + \frac{1}{\sqrt{N}} \right\}.$$

Choosing as $c = 1/\sqrt{N}$, we obtain $\widehat{\mathcal{R}}(\mathcal{G}) \lesssim 1/\sqrt{N}$. This bound is the displayed inequality of this lemma. \square

Proof of Lemma 4. The proof of Lemma 4 is almost the same as that of Lemma 3. In fact, since $\|\mathbf{y}_{\tau_i,j}\|_2$ is bounded from the assumption, we have

$$\begin{aligned} &\mathbb{E}_{\tau,\sigma} \left[\sup_{f \in \mathcal{F}} \frac{1}{N} \sum_{i=1}^N \sigma_i \langle f(\mathbf{y}_{0,j}, \tau_i), \mathbf{y}_{\tau_i,j} \rangle_2 \right] \\ &\leq B_2 \sum_{k=1}^d \mathbb{E}_{\tau,\sigma} \left[\sup_{f_k \in \mathcal{F}_k} \frac{1}{N} \sum_{i=1}^N \sigma_i (B_2^{-1} \mathbf{y}_{\tau_i,j,k}) f_k(\mathbf{y}_{0,j}, \tau_i) \right], \end{aligned}$$

where $\mathcal{F}_k = \{f_k | f = (f_1, \dots, f_k, \dots, f_d) \in \mathcal{F}\}$, and $\mathbf{y}_{\tau_i,j} = (\mathbf{y}_{\tau_i,j,1}, \dots, \mathbf{y}_{\tau_i,j,d})$. Since $B_2^{-1} \mathbf{y}_{\tau_i,j,k} \leq 1$ from the assumption that $\|\mathbf{y}_{\tau_i,j}\|_2 \leq B_2$ holds almost surely, the rescaled function $(B_2^{-1} \mathbf{y}_{\tau_i,j,k}) f_k(\cdot, \cdot)$ is also L -Lipschitz continuous. By Theorem 12 in [37] which shows the monotonicity of $\widehat{\mathcal{R}}$, we have

$$\mathbb{E}_{\sigma} \left[\sup_{f_k \in \mathcal{F}_k} \frac{1}{N} \sum_{i=1}^N \sigma_i (B_2^{-1} \mathbf{y}_{\tau_i,j,k}) f_k(\mathbf{y}_{0,j}, \tau_i) \right] \leq \widehat{\mathcal{R}}(\mathcal{F}_k).$$

Therefore, by Lemma 5 due to [36], Corollary 4.2.13 in [39], and some calculation based on Example 4 in [36], as in the proof of Lemma 3, we obtain the claim. \square

References

- [1] Kostadin Dabov, Alessandro Foi, Vladimir Katkovnik, and Karen Egiazarian. Image denoising by sparse 3-D transform-domain collaborative filtering. *IEEE Transactions on Image Processing*, 16(8):2080–2095, 2007. doi: 10.1109/tip.2007.901238. 1, 12
- [2] Kai Zhang, Wangmeng Zuo, Yunjin Chen, Deyu Meng, and Lei Zhang. Beyond a Gaussian denoiser: Residual learning of deep CNN for image denoising. *IEEE Transactions on Image Processing*, 26(7):3142–3155, 2017. doi: 10.1109/tip.2017.2662206. 1, 2

- [3] Jaakko Lehtinen, Jacob Munkberg, Jon Hasselgren, Samuli Laine, Tero Karras, Miika Aittala, and Timo Aila. Noise2Noise: Learning image restoration without clean data. In *Proceedings of the 35th International Conference on Machine Learning*, volume 80 of *Proceedings of Machine Learning Research*, pages 2965–2974. PMLR, 10–15 Jul 2018. [1](#), [2](#), [3](#), [4](#), [5](#), [6](#), [7](#), [8](#), [10](#), [15](#)
- [4] Alexander Krull, Tim-Oliver Buchholz, and Florian Jug. Noise2Void - learning denoising from single noisy images. In *2019 IEEE/CVF Conference on Computer Vision and Pattern Recognition (CVPR)*, pages 2124–2132, 2019. doi: 10.1109/CVPR.2019.00223. [2](#), [4](#), [5](#)
- [5] Tao Huang, Songjiang Li, Xu Jia, Huchuan Lu, and Jianzhuang Liu. Neighbor2Neighbor: Self-supervised denoising from single noisy images. In *2021 IEEE/CVF Conference on Computer Vision and Pattern Recognition (CVPR)*, pages 14776–14785, 2021. doi: 10.1109/CVPR46437.2021.01454. [2](#), [4](#), [5](#), [6](#), [7](#), [10](#)
- [6] Yuhui Quan, Mingqin Chen, Tongyao Pang, and Hui Ji. Self2Self with dropout: Learning self-supervised denoising from single image. In *2020 IEEE/CVF Conference on Computer Vision and Pattern Recognition (CVPR)*, pages 1887–1895, 2020. doi: 10.1109/CVPR42600.2020.00196. [2](#), [3](#), [4](#), [5](#), [10](#)
- [7] Youssef Mansour and Reinhard Heckel. Zero-shot Noise2Noise: Efficient image denoising without any data. In *Proceedings of the IEEE/CVF Conference on Computer Vision and Pattern Recognition (CVPR)*, pages 14018–14027, June 2023. [2](#), [4](#)
- [8] Magauiya Zhussip, Shakarim Soltanayev, and Se Young Chun. Extending Stein's unbiased risk estimator to train deep denoisers with correlated pairs of noisy images. In *Advances in Neural Information Processing Systems*, volume 32. Curran Associates, Inc., 2019. [2](#), [7](#)
- [9] Lesley A Earl, Veronica Falconieri, Jacqueline LS Milne, and Sriram Subramaniam. Cryo-EM: beyond the microscope. *Current Opinion in Structural Biology*, 46:71–78, October 2017. [2](#)
- [10] Dmitry Lyumkis. Challenges and opportunities in cryo-EM single-particle analysis. *Journal of Biological Chemistry*, 294(13):5181–5197, March 2019. [2](#)
- [11] Sjors H.W. Scheres. Relion: Implementation of a bayesian approach to cryo-em structure determination. *Journal of Structural Biology*, 180(3):519–530, 2012. [2](#), [13](#)
- [12] Ali Punjani, John L Rubinstein, David J Fleet, and Marcus A Brubaker. cryoSPARC: Algorithms for rapid unsupervised cryo-EM structure determination. *Nature Methods*, 14(3): 290–296, 2017. [2](#), [13](#)
- [13] Junjie Yuan, Kangjing Chen, Wenbo Zhang, and Zhucheng Chen. Structure of human chromatin-remodelling PBAF complex bound to a nucleosome. *Nature*, 605(7908):166–171, 2022. [2](#)

- [14] Junshen Xu and Elfar Adalsteinsson. Deformed2Self: Self-supervised denoising for dynamic medical imaging. In *Medical Image Computing and Computer Assisted Intervention – MICCAI 2021*, pages 25–35, Cham, 2021. Springer International Publishing. doi: 10.1007/978-3-030-87196-3_3. [2](#), [3](#), [5](#), [6](#), [10](#), [12](#)
- [15] Weijie Gan, Yu Sun, Cihat Eldeniz, Jiaming Liu, Hongyu An, and Ulugbek S. Kamilov. Deformation-compensated learning for image reconstruction without ground truth. *IEEE Transactions on Medical Imaging*, 41(9):2371–2384, 2022. doi: 10.1109/TMI.2022.3163018. [2](#), [5](#), [6](#)
- [16] Thibaud Ehret, Axel Davy, Pablo Arias, and Gabriele Facciolo. Joint demosaicking and denoising by fine-tuning of bursts of raw images. In *2019 IEEE/CVF International Conference on Computer Vision (ICCV)*. IEEE, 2019. doi: 10.1109/iccv.2019.00896. [2](#), [5](#), [6](#)
- [17] Joshua Batson and Loic Royer. Noise2Self: Blind denoising by self-supervision. In *Proceedings of the 36th International Conference on Machine Learning*, volume 97 of *Proceedings of Machine Learning Research*, pages 524–533. PMLR, 09–15 Jun 2019. [4](#)
- [18] Nick Moran, Dan Schmidt, Yu Zhong, and Patrick Coady. Noisier2Noise: Learning to denoise from unpaired noisy data. In *2020 IEEE/CVF Conference on Computer Vision and Pattern Recognition (CVPR)*, pages 12061–12069, 2020. doi: 10.1109/CVPR42600.2020.01208. [4](#), [9](#)
- [19] Tongyao Pang, Huan Zheng, Yuhui Quan, and Hui Ji. Recorruped-to-Recorruped: Unsupervised deep learning for image denoising. In *2021 IEEE/CVF Conference on Computer Vision and Pattern Recognition (CVPR)*, pages 2043–2052, 2021. doi: 10.1109/CVPR46437.2021.00208. [4](#), [9](#)
- [20] Zejin Wang, Jiazheng Liu, Guoqing Li, and Hua Han. Blind2unblind: Self-supervised image denoising with visible blind spots. In *2022 IEEE/CVF Conference on Computer Vision and Pattern Recognition (CVPR)*, pages 2017–2026, 2022. doi: 10.1109/CVPR52688.2022.00207. [4](#)
- [21] Wooseok Lee, Sanghyun Son, and Kyoung Mu Lee. AP-BSN: Self-supervised denoising for real-world images via asymmetric PD and blind-spot network. In *2022 IEEE/CVF Conference on Computer Vision and Pattern Recognition (CVPR)*, pages 17704–17713, 2022. doi: 10.1109/CVPR52688.2022.01720. [4](#)
- [22] Gregory Vaksman and Michael Elad. Patch-craft self-supervised training for correlated image denoising. In *Proceedings of the IEEE/CVF Conference on Computer Vision and Pattern Recognition (CVPR)*, pages 5795–5804, June 2023. [4](#)
- [23] Jiachuan Wang, Shimin Di, Lei Chen, and Charles Wang Wai Ng. Noise2Info: Noisy image to information of noise for self-supervised image denoising. In *Proceedings of the IEEE/CVF International Conference on Computer Vision (ICCV)*, pages 16034–16043, October 2023. [4](#)

- [24] Yizhong Pan, Xiao Liu, Xiangyu Liao, Yuanzhouhan Cao, and Chao Ren. Random sub-samples generation for self-supervised real image denoising. In *Proceedings of the IEEE/CVF International Conference on Computer Vision (ICCV)*, pages 12150–12159, October 2023. [4](#)
- [25] Tristan Bepler, Kotaro Kelley, Alex J. Noble, and Bonnie Berger. Topaz-Denoise: general deep denoising models for cryoEM and cryoET. *Nature Communications*, 11(1), 2020. doi: 10.1038/s41467-020-18952-1. [4](#)
- [26] Hao Chen, Chenyuan Qu, Yu Zhang, Chen Chen, and Jianbo Jiao. Multi-view self-supervised disentanglement for general image denoising. In *Proceedings of the IEEE/CVF International Conference on Computer Vision (ICCV)*, pages 12281–12291, October 2023. [4](#)
- [27] Victor Lempitsky, Andrea Vedaldi, and Dmitry Ulyanov. Deep image prior. In *2018 IEEE/CVF Conference on Computer Vision and Pattern Recognition*, pages 9446–9454, 2018. doi: 10.1109/CVPR.2018.00984. [4](#)
- [28] Jason Lequyer, Reuben Philip, Amit Sharma, Wen-Hsin Hsu, and Laurence Pelletier. A fast blind zero-shot denoiser. *Nature Machine Intelligence*, 4:953–963, 2022. doi: 10.1038/s42256-022-00547-8. [4](#), [12](#)
- [29] Calvin-Khang Ta, Abhishek Aich, Akash Gupta, and Amit K. Roy-Chowdhury. Poisson2Sparse: Self-supervised Poisson denoising from a single image. In *Medical Image Computing and Computer Assisted Intervention – MICCAI 2022*, pages 557–567, Cham, 2022. Springer Nature Switzerland. doi: 10.1007/978-3-031-16452-1_53. [4](#)
- [30] Ben Mildenhall, Jonathan T. Barron, Jiawen Chen, Dillon Sharlet, Ren Ng, and Robert Carroll. Burst denoising with kernel prediction networks. In *2018 IEEE/CVF Conference on Computer Vision and Pattern Recognition*, pages 2502–2510, 2018. doi: 10.1109/CVPR.2018.00265. [5](#)
- [31] Clément Godard, Kevin Matzen, and Matt Uyttendaele. Deep burst denoising. In *Computer Vision – ECCV 2018*, pages 560–577. Springer International Publishing, 2018. doi: 10.1007/978-3-030-01267-0_33. [5](#)
- [32] Akshay Dudhane, Syed Waqas Zamir, Salman Khan, Fahad Shahbaz Khan, and Ming-Hsuan Yang. Burst image restoration and enhancement. In *2022 IEEE/CVF Conference on Computer Vision and Pattern Recognition (CVPR)*, pages 5749–5758, 2022. doi: 10.1109/CVPR52688.2022.00567. [5](#)
- [33] Jonathan Ho, Ajay Jain, and Pieter Abbeel. Denoising diffusion probabilistic models. In *Advances in Neural Information Processing Systems*, volume 33, pages 6840–6851. Curran Associates, Inc., 2020. [5](#), [6](#)
- [34] Tiange Xiang, Mahmut Yurt, Ali B Syed, Kawin Setsompop, and Akshay Chaudhari. DDM²: Self-supervised diffusion MRI denoising with generative diffusion models. In

- The Eleventh International Conference on Learning Representations*, 2023. URL <https://openreview.net/forum?id=0vqjc50HfcC>. 6
- [35] Trevor Hastie, Robert Tibshirani, and Jerome H Friedman. *The elements of statistical learning: data mining, inference, and prediction*. Springer, second edition, 2009. 6, 17
 - [36] Ulrike von Luxburg and Olivier Bousquet. Distance-based classification with Lipschitz functions. *Journal of Machine Learning Research*, 5(Jun):669–695, 2004. 7, 24, 25
 - [37] Peter L. Bartlett and Shahar Mendelson. Rademacher and Gaussian complexities: Risk bounds and structural results. *Journal of Machine Learning Research*, 3(Nov):463–482, 2002. 7, 18, 24, 25
 - [38] Mehryar Mohri, Afshin Rostamizadeh, and Ameet Talwalkar. *Foundations of machine learning*. MIT press, second edition, 2018. 7, 18, 20, 21, 22, 23, 24
 - [39] Roman Vershynin. *High-Dimensional Probability: An Introduction with Applications in Data Science*. Cambridge Series in Statistical and Probabilistic Mathematics. Cambridge University Press, 2018. doi: 10.1017/9781108231596. 7, 24, 25
 - [40] Jun Xu, Yuan Huang, Ming-Ming Cheng, Li Liu, Fan Zhu, Zhou Xu, and Ling Shao. Noisy-as-Clean: Learning self-supervised denoising from corrupted image. *IEEE Transactions on Image Processing*, 29:9316–9329, 2020. doi: 10.1109/TIP.2020.3026622. 9
 - [41] Melody G Campbell, Anchi Cheng, Axel F Brilot, Arne Moeller, Dmitry Lyumkis, David Veesler, Junhua Pan, Stephen C Harrison, Clinton S Potter, Bridget Carragher, and Nikolaus Grigorieff. Movies of ice-embedded particles enhance resolution in electron cryo-microscopy. *Structure*, 20(11):1823–1828, November 2012. 9
 - [42] Shawn Q Zheng, Eugene Palovcak, Jean-Paul Armache, Kliment A Verba, Yifan Cheng, and David A Agard. MotionCor2: anisotropic correction of beam-induced motion for improved cryo-electron microscopy. *Nature Methods*, 14(4):331–332, April 2017. 9
 - [43] Nitish Srivastava, Geoffrey Hinton, Alex Krizhevsky, Ilya Sutskever, and Ruslan Salakhutdinov. Dropout: A simple way to prevent neural networks from overfitting. *Journal of Machine Learning Research*, 15(56):1929–1958, 2014. 10
 - [44] Alain Horé and Djemel Ziou. Image quality metrics: Psnr vs. ssim. In *2010 20th International Conference on Pattern Recognition*, pages 2366–2369, 2010. doi: 10.1109/ICPR.2010.579. 10
 - [45] Zhou Wang, A.C. Bovik, H.R. Sheikh, and E.P. Simoncelli. Image quality assessment: from error visibility to structural similarity. *IEEE Transactions on Image Processing*, 13(4):600–612, 2004. doi: 10.1109/TIP.2003.819861. 10

- [46] Stéfan van der Walt, Johannes L. Schönberger, Juan Nunez-Iglesias, François Boulogne, Joshua D. Warner, Neil Yager, Emmanuelle Gouillart, Tony Yu, and the scikit-image contributors. scikit-image: image processing in python. *PeerJ*, 2:e453, 2014. [10](#)
- [47] Wesley Khademi, Sonia Rao, Clare Minnerath, Guy Hagen, and Jonathan Ventura. Self-supervised Poisson-Gaussian denoising. In *2021 IEEE Winter Conference on Applications of Computer Vision (WACV)*. IEEE, 2021. doi: 10.1109/wacv48630.2021.00218. [10](#), [11](#), [12](#)
- [48] Olivier Bernard, Alain Lalande, Clement Zotti, Frederick Cervenansky, Xin Yang, Pheng-Ann Heng, Irem Cetin, Karim Lekadir, Oscar Camara, Miguel Angel Gonzalez Ballester, Gerard Sanroma, Sandy Napel, Steffen Petersen, Georgios Tziritas, Elias Grinias, Mahendra Khened, Varghese Alex Kollerathu, Ganapathy Krishnamurthi, Marc-Michel Rohé, Xavier Pennec, Maxime Sermesant, Fabian Isensee, Paul Jäger, Klaus H. Maier-Hein, Peter M. Full, Ivo Wolf, Sandy Engelhardt, Christian F. Baumgartner, Lisa M. Koch, Jelmer M. Wolterink, Ivana Išgum, Yeonggul Jang, Yoonmi Hong, Jay Patravali, Shubham Jain, Olivier Humbert, and Pierre-Marc Jodoin. Deep learning techniques for automatic MRI cardiac multi-structures segmentation and diagnosis: Is the problem solved? *IEEE Transactions on Medical Imaging*, 37(11):2514–2525, 2018. doi: 10.1109/TMI.2018.2837502. [12](#)
- [49] Ymir Mäkinen, Lucio Azzari, and Alessandro Foi. “bm3d”. Python Package Index, 2022. URL <https://pypi.org/project/bm3d/> [Last accessed on 5th February, 2024]. [12](#)
- [50] Ymir Mäkinen, Lucio Azzari, and Alessandro Foi. Collaborative filtering of correlated noise: Exact transform-domain variance for improved shrinkage and patch matching. *IEEE Transactions on Image Processing*, 29:8339–8354, 2020. doi: 10.1109/TIP.2020.3014721. [12](#)
- [51] Jason Lequyer, Reuben Philip, Amit Sharma, Wen-Hsin Hsu, and Laurence Pelletier. “jason-lequyer/Noise2Fast”. GitHub, 2023. URL: <https://github.com/jason-lequyer/Noise2Fast> [Last accessed on 5th February, 2024]. [12](#)
- [52] Junshen Xu and Elfar Adalsteinsson. “daviddmc/Deform2Self”. GitHub, 2022. URL: <https://github.com/daviddmc/Deform2Self> [Last accessed on 5th February, 2024]. [12](#)
- [53] Andrii Iudin, Paul K Korir, Sriram Somasundharam, Simone Weyand, Cesare Cattavittello, Neli Fonseca, Osman Salih, Gerard J Kleywegt, and Ardan Patwardhan. EMPIAR: the electron microscopy public image archive. *Nucleic Acids Research*, 51(D1):D1503–D1511, January 2023. [13](#)
- [54] Johannes Schindelin, Ignacio Arganda-Carreras, Erwin Frise, Verena Kaynig, Mark Longair, Tobias Pietzsch, Stephan Preibisch, Curtis Rueden, Stephan Saalfeld, Benjamin Schmid, Jean-Yves Tinevez, Daniel James White, Volker Hartenstein, Kevin Eliceiri, Pavel Tomančák, and Albert Cardona. Fiji: an open-source platform for biological-image analysis. *Nature Methods*, 9(7):676–682, June 2012. [15](#)

- [55] Adam Paszke, Sam Gross, Francisco Massa, Adam Lerer, James Bradbury, Gregory Chanan, Trevor Killeen, Zeming Lin, Natalia Gimelshein, Luca Antiga, Alban Desmaison, Andreas Kopf, Edward Yang, Zachary DeVito, Martin Raison, Alykhan Tejani, Sasank Chilamkurthy, Benoit Steiner, Lu Fang, Junjie Bai, and Soumith Chintala. Pytorch: An imperative style, high-performance deep learning library. In *Advances in Neural Information Processing Systems*, volume 32. Curran Associates, Inc., 2019. [15](#)
- [56] Olaf Ronneberger, Philipp Fischer, and Thomas Brox. U-net: Convolutional networks for biomedical image segmentation. In *Medical Image Computing and Computer-Assisted Intervention – MICCAI 2015*, pages 234–241, Cham, 2015. Springer International Publishing. doi: 10.1007/978-3-319-24574-4_28. [15](#)
- [57] Diederik P. Kingma and Jimmy Ba. Adam: A method for stochastic optimization. In *3rd International Conference on Learning Representations, ICLR 2015*, 2015. [16](#)